Aqueous alteration processes in Jezero crater, Mars - implications for organic geochemistry

Eva L. Scheller[1,2]†* & Joseph Razzell Hollis[3,4]†, Emily L. Cardarelli[3], Andrew Steele[5], Luther W. Beegle[3], Rohit Bhartia[6], Pamela Conrad[5], Kyle Uckert[3], Sunanda Sharma[3], Bethany L. Ehlmann[1], William J. Abbey[3], Sanford A. Asher[7], Kathleen C. Benison[8], Eve L. Berger[9,10,11], Olivier Beyssac[12], Benjamin L. Bleefeld[13], Tanja Bosak[2], Adrian J. Brown[14], Aaron S. Burton[11], Sergei V. Bykov[7], Ed Cloutis[15], Alberto G. Fairén[16,17], Lauren DeFlores[3], Kenneth A. Farley[1], Deidra M. Fey[13], Teresa Fornaro[17], Allison C. Fox[11], Marc Fries[11], Keyron Hickman-Lewis[19,20], William F. Hug[6], Joshua E. Huggett[13], Samara Imbeah[13], Ryan S. Jakubek[11], Linda C. Kah[21], Peter Kelemen[22], Megan R. Kennedy[13], Tanya Kizovski[23], Carina Lee[24], Yang Liu[3], Lucia Mandon[25], Francis M. McCubbin[11], Kelsey R. Moore[3], Brian E. Nixon[13], Jorge I. Núñez[26], Carolina Rodriguez Sanchez-Vahamonde[13], Ryan D. Roppel[7], Mitchell Schulte[27], Mark A. Sephton[28], Shiv K. Sharma[29], Sandra Siljeström[30], Svetlana Shkolyar[31,32], David L. Shuster[33], Justin I. Simon[11], Rebecca J. Smith[34], Kathryn M. Stack[3], Kim Steadman[3], Benjamin P. Weiss[2], Alyssa Werynski[13], Amy J. Williams[35], Roger C. Wiens[36], Kenneth H. Williford[3,37], Kathrine Winchell[13], Brittan Wogsland[21], Anastasia Yanchilina[38], Rachel Yingling[13], and Maria-Paz Zorzano[16]

Affiliations:
†These authors contributed equally to this work.
[1]Division of Geological and Planetary Sciences, California Institute of Technology; Pasadena, CA, USA.
[2]Department of Earth, Atmospheric, and Planetary Sciences, Massachusetts Institute of Technology, Cambridge, MA, USA.
[3]NASA Jet Propulsion Laboratory, California Institute of Technology; Pasadena, CA, USA.
[4]The Natural History Museum, London, United Kingdom
[5]Earth and Planets Laboratory, Carnegie Institution for Science; Washington, DC, USA.
[6]Photon Systems Incorporated; Covina, CA, USA.
[7]Department of Chemistry, University of Pittsburgh, Pittsburgh, PA, USA.
[8]Department of Geology and Geography, West Virginia University, Morgantown, WV, USA.
[9]Texas State University, San Marcos, TX, USA
[10]Jacobs JETS, Houston, TX, USA
[11]NASA Johnson Space Center, Houston, TX, USA.
[12]Institut de Minéralogie, de Physique des Matériaux et de Cosmochimie, Centre National de la Recherche Scientifique, Sorbonne Université, Muséum National d'Histoire Naturelle, 75005 Paris, France.
[13]Malin Space Science Systems, San Diego, CA, USA.
[14]Plancus Research, Severna Park, MD, USA.
[15]Geography, The University of Winnipeg, Winnipeg, Canada.

39   [16]Centro de Astrobiología (CSIC-INTA), Madrid, Spain.

40   [17]Department of Astronomy, Cornell University, Ithaca, NY, USA

41   [18]INAF-Astrophysical Observatory of Arcetri, Florence, Italy.

42   [19]Department of Earth Sciences, The Natural History Museum, London, United Kingdom.

43   [20]Dipartimento di Scienze Biologiche, Geologiche e Ambientali, Università di Bologna,

44   Bologna, Italy.

45   [21]Department of Earth and Planetary Sciences, University of Tennesee, Knoxville, TN, USA.

46   [22]Lamont Doherty Earth Observatory, Columbia University, Palisades, NY, USA.

47   [23]Department of Earth Sciences, Brock University, St. Catharines, ON L2S 3A1, Canada.

48   [24]Lunar & Planetary Institute, Universities Space Research Association, Houston, TX, USA.

49   [25]Laboratoire d'Etudes Spatiales et d'Instrumentation en Astrophysique, Observatoire de

50   Paris, Centre National de la Recherche Scientifique, Sorbonne Université, Université Paris

51   Diderot, 92195 Meudon, France.

52   [26]Johns Hopkins University Applied Physics Laboratory, Laurel, MD, USA.

53   [27]Mars Exploration Program, NASA Headquarters, Washington, DC, USA.

54   [28]Earth Science and Engineering, South Kensington Campus, Imperial College London, SW7

55   2AZ, United Kingdom.

56   [29]Hawaii Institute of Geophysics and Planetology, University of Hawaii at Manoa, Honolulu,

57   HI-96822, USA.

58   [30]RISE Research Institutes of Sweden, Stockholm, Sweden.

59   [31]University of Maryland, College Park, MD, USA.

60   [32]NASA Goddard Space Flight Center, Greenbelt, MD, USA.

61   [33]Earth and Planetary Science, University of California Berkeley, Berkeley, CA, USA.

62   [34]Department of Geosciences, Stony Brook University, Stony Brook, NY, USA.

63   [35]Department of Geological Sciences, University of Florida, Gainesville, FL, USA.

64   [36]Los Alamos National Laboratory, Los Alamos, NM, USA.

65   [37]Blue Marble Space Institute of Science, Seattle, WA, USA.

66   [38]Impossible Sensing, St. Louis, MO, USA.

67   *Corresponding author. Email: eschelle@mit.edu

68

69   **Abstract:** The Perseverance rover landed in Jezero crater, Mars in February 2021. We used the

70   Scanning Habitable Environments with Raman and Luminescence for Organics and Chemicals

71   (SHERLOC) instrument to perform deep ultraviolet Raman and fluorescence spectroscopy of

72   three rocks within the crater. We identify evidence for two ancient aqueous environments. Liquid

73   water formed carbonates in an olivine-rich igneous rock. A sulfate-perchlorate mixture is present

74   in the rocks, probably formed by later modifications of the rocks by brine. Fluorescence

75   signatures consistent with aromatic organic compounds occur throughout these rocks, preserved

76   in minerals related to both aqueous environments.

77

78

Main text:

The Perseverance rover landed in Jezero crater, Mars to investigate the geology of the crater, identify habitable environments, assess whether life ever existed on Mars, and to collect samples for potential return to Earth *(1)*. Jezero hosted an open-basin lake during the Noachian (~3.7 Ga) *(1-2)*, units associated with the largest carbonate deposit identified on Mars *(2-4)*, and a well-preserved delta with clay and carbonate-bearing sediments, well-suited to preservation of organics *(1)*. Organics have previously been detected on Mars *(5,6)*, and here we resolve the spatial and mineralogical context of organics in Jezero crater with the rover's SHERLOC instrument (Scanning Habitable Environments with Raman and Luminescence for Organics and Chemicals), a deep-ultraviolet fluorescence and Raman spectrometer capable of mapping organic and mineral composition with a spatial resolution of 100 μm *(7)*. Complementary elemental chemistry analyses are performed by the PIXL (Planetary Instrument for X-ray Lithochemistry) and SuperCam instruments *(8-11)*.

We report the presence of organics and aqueously formed minerals at Jezero crater in three rock targets [8] analyzed during the first 208 sols of the mission (Fig. 1) located in two different orbitally and rover-identified geological units within the floor of Jezero crater *(9,12)*. The Garde target is from the altered ultramafic Séítah Formation (Fm), orbitally mapped as the Crater Floor Fractured 1 unit (CF-f1) (Fig. 1) *(9,12)*. The Guillaumes and Bellegarde targets are from the overlying and therefore younger basaltic Máaz Fm, orbitally mapped as the ~2.3-2.6 Ga *(13)* Crater Floor Fractured Rough unit (CF-fr) *(9,12)*. The Perseverance rover drilled four rock samples from the Séítah Fm. Montdenier and Montagnac rock samples were obtained from the Bellegarde rock, while the Guillaumes rock sample attempt, Roubion, failed *(12)*. These rock samples are planned to be returned to Earth.

All three Raman spectral scans *(8)* from Garde exhibit strong peaks that have a peak position range of 1080 to 1090 cm^{-1} (n=38) attributed to carbonate (spectrum 1 and ROI 1-4 in Fig. 2H), and peaks with a peak position range of 820 to 840 cm^{-1} (n=60) attributed to olivine (ROI 1 and 4 in Fig. 2H) *(8,13-14)*. Olivines were found to be more Fe-rich than laboratory measured olivines of Fo# 80-90, while carbonates are likely mixed Fe- and Mg-species based on 1080-1087 cm^{-1} peak positions *(8)* and Ca-dominated species are excluded based on PIXL data *(11)*. These spectral detections were overlaid on Wide-Angle Topographic Sensor for Operations and eNgineering (WATSON) camera images to correlate spectral position with textures *(8)*. Olivine and carbonate are associated with μm- to mm-sized light-toned tan, reddish-brown, and dark-toned sub-angular grains as well as light-toned intergranular spaces (Fig. 2.B,E). Spectral features of olivines and carbonates often co-occur in a single spectrum; however, there are also areas where either olivine or carbonate occur independently. Spectral observations of a weak, broad Raman peak centered ~1060 cm^{-1} (FWHM ~200 cm^{-1}) may indicate a disordered phase

116   consistent with amorphous silicates, often difficult to detect given their low intensity (Fig. 2). A
117   peak at 960±5 cm^{-1} is likely phosphate, although perchlorates cannot be excluded (Fig. 2).

118   Garde detail scans *(8)* exhibit strong fluorescence signatures, centralized at ~340 nm, that
119   spatially correlate with carbonate, probable phosphate, and amorphous silicate spectra localized
120   within narrow intergranular spaces (Fig. 2.E-F). A less intense fluorescence band centered at 285
121   nm typically accompanies the 340 nm fluorescence. Other areas exhibit no fluorescence (Fig.
122   2.C).
123
124   Guillaumes features white and reddish brown, anhedral patches, 1-2 mm across (Fig. 3.A, S1).
125   These are secondary materials within a basaltic igneous rock *(9)* interpreted as void fills and
126   correlate with sulfate and perchlorate spectra. Spectra with high intensity 950-955 cm^{-1} peaks
127   and minor 1090-1095 cm^{-1} and 1150-1155 cm^{-1} peaks match laboratory measurements of
128   anhydrous Na-perchlorate *(8)* (Fig. 3.G, S4). Two strong Na-perchlorate detections correlate
129   with centers of the brightest material within the anhedral patches *(8)*. Guillaumes spectra
130   commonly contain a single low-intensity peak positioned at 950-955 cm^{-1}. We interpret these as
131   low intensity Na-perchlorate peaks, although the cation species is uncertain due to a lack of
132   resolvable minor peaks *(8)* (Fig. 3.G). Other spectra exhibit both 950-955 cm^{-1} peaks and
133   equally strong 1010-1020 cm^{-1} peaks, with low intensity broad features at 1120±5 cm^{-1}, and
134   occasional broad 3450±5 cm^{-1} hydration features, consistent with a mixture of sulfate and
135   perchlorate that is minimally hydrated (Fig. 3.G). A Ca-sulfate species best explains these
136   spectra when coupled with elemental chemistry data from PIXL and SuperCam *(8)*. Last, two
137   detected 965 cm^{-1} peaks are likely phosphates, although perchlorates cannot be excluded.

139   Bellegarde contains white 0.5-1 mm anhedral to sub-euhedral secondary crystals that have a
140   reddish brown semi-isopachous rim interpreted as void fills within a basaltic igneous rock *(8)*
141   (Fig. S2). These crystals exhibit 1010-1020 cm^{-1} peaks, similarly attributed to Ca-sulfate when
142   coupled with elemental chemistry data *(8)*. Several of the sulfate peaks are also associated with a
143   narrow low-intensity hydration feature at 3560±5 cm^{-1}, consistent with hydrated Ca-sulfates
144   (Fig. S3). The Bellegarde target contains a single 1080±5 cm^{-1} peak of possible Ca-carbonate
145   (Fig. 4, S2). Narrow peaks at 975 cm^{-1} peak could not definitively be identified and could be
146   phosphate or perchlorate *(8)*. The SHERLOC mineral detections within the Bellegarde and
147   Guillaumes targets are consistent with the results from other Perseverance instruments *(8-9,11)*
148   (Fig. S5-S6).

150   Guillaumes and Bellegarde targets commonly exhibit a weak, broad fluorescence feature with a
151   maximum at ~340 nm (Fig. 3D, 4D) that appears to be widely distributed across each surface and
152   is occasionally correlated with reddish-brown materials. Although this feature sometimes co-
153   occurs with perchlorate, sulfate, and possibly phosphate, it occurs equally often in areas with
154   unidentified mineralogy. Bellegarde has two other signatures at ~275 and ~305 nm (blue and

155 green respectively in Fig. 4D), which are strong and localized on specific, light-toned features.
156 The ~305 nm signature is associated with detected sulfate (Fig. 4.D-F, S2). In Guillaumes, a
157 second fluorescence signature at ~275 nm (Fig. 3D) is observed in two locations, approximately
158 300 μm in diameter, coincident with previous SuperCam laser spots *(8)*.
159

160 Observation of olivine and carbonate mixtures within the Garde target of the Séítah Fm is
161 consistent with orbital infrared observations *(2-4)* and substantiated by multiple lines of evidence
162 *(9-11)*. Previously proposed hypotheses for the precipitation of these carbonates include low-
163 temperature and high-temperature aqueous alteration of an olivine-rich protolith *(3,15-17)* or
164 authigenic precipitation from lake or groundwater *(4,15-17)*. Our 10-100 μm-scale textural and
165 spectroscopic evidence supports carbonate formation through aqueous alteration of an ultramafic
166 protolith, known as carbonation. The supporting evidence includes: (i) Carbonate cation
167 compositions consistent with those of olivines, suggesting mixed Fe- and Mg-olivine gave rise to
168 mixed Fe- and Mg-carbonates, similar to on Earth and within Martian meteorites *(16,18-19)*. (ii)
169 The observed carbonates co-occur with hydrated materials *(9)* and potentially aqueously formed
170 amorphous silicates and phosphate. (iii) The spectral and textural variation of olivine and
171 carbonate dominated zones within both primary grains and intergranular spaces are expected for
172 carbonated ultramafic protoliths on Earth (reviewed in *(16)*) and within Martian meteorites *(18-*
173 *19)*.

174 These observations suggest that the degree of aqueous alteration to the ultramafic protolith was
175 relatively low since large olivine-rich domains remain intact, although the alteration is pervasive
176 and occurs throughout the primary lithology rather than in specific spatial domains, e.g.,
177 fractures. In ultramafic alteration environments on Earth *(16)* and in Martian meteorites *(18-19)*,
178 carbonation can be associated with the formation of oxides, hydroxides, and/or Fe/Mg-rich
179 phyllosilicates, which have not been observed *(9)*. Carbonation can occur in a wide range of
180 temperatures from low to ambient to hydrothermal/metamorphic *(15-17)*. Other alteration
181 minerals, such as serpentine, have not been definitively observed in the Séítah Fm to date, which
182 may suggest time limited interactions, low water rock ratios, or ambient fluid temperatures
183 during carbonation *(3,15-17)*.

184 The similarity between the mineralogy of the Garde target in the Séítah Fm to the surrounding
185 widespread, regional olivine-carbonate-bearing unit with a similar orbital spectroscopic signature
186 and geomorphological texture *(3-4,15-16)* suggests that carbonation of olivine may have
187 occurred throughout this extensive region on ancient Mars (~2.7-3.8 Ga). These observations
188 parallel those made by the Spirit rover in Gusev Crater *(20)* and within (1.3-4 Ga) Martian
189 meteorites *(18-19)*. Previous modeling efforts have suggested that carbonate deposition could
190 have played a role in the evolution of Mars' atmosphere *(3,17,22)*, but the geological nature of
191 such a depositional mechanism had remained unexplained. Taken together, micron-scale

192   SHERLOC observations of this phenomenon bridges previous orbital and meteorite observations
193   and demonstrates ultramafic alteration resulting in geological deposition of carbonates.

194
195   Jezero crater perchlorate detections, like the initial Phoenix observations *(23)*, are substantiated
196   by three independent instruments *(9)*. Previous evidence for Martian perchlorates includes
197   observations by the Curiosity rover *(24)*, proposed but later disputed orbital detections within
198   recurring slope lineae *(25)*, and detection within the Tissint meteorite *(26)*. The SHERLOC
199   perchlorate detections differ from previous mission observations because they are observed
200   within the interior of a rock and not on the surface, are related to aqueous processes, and are
201   likely Na-perchlorate as compared to previously detected Ca-, Fe- or Mg-perchlorates *(24)*.

202   Previous hypotheses for perchlorate formation on Mars are (i) irradiation of chlorine-bearing
203   parent minerals *(37)*, (ii) atmospheric oxidation of chlorine species *(28)*, or (iii) formation from
204   brines *(26)*. Perchlorates may also be mobilized in thin films of fluid *(24)*. The Jezero
205   perchlorates form white void-fills within rock interiors, and did not form directly on the surface
206   as expected from materials formed by cosmic irradiation or atmospheric oxidation, indicating
207   either formation or mobilization through briny fluids after basalt formation. The concomitant
208   detection of sulfates and perchlorates within the Guillaumes target suggests that sulfate formed
209   together with perchlorate or parent chlorine-bearing species, such as halite, within percolating
210   briny waters that were then subsequently oxidized to perchlorate. Bellegarde exhibited sulfate
211   without perchlorate, suggesting these brines did not precipitate chlorine-bearing parent species,
212   that perchlorate formation was not pervasive, or that perchlorates were since dissolved.
213   Perchlorates are easily dissolved, and therefore perchlorates likely formed when these rocks were
214   last exposed to liquid water. Perchlorate and sulfate detections within the stratigraphically
215   younger Máaz Fm *(9)* substantiates an aqueous environment on Mars that occurred separately
216   from the stratigraphically older *(9)* Séítah Fm carbonation environment.

217
218   Deep ultraviolet (DUV) fluorescence is particularly sensitive to aromatic organic compounds,
219   and the fluorescence signatures observed in all three targets are consistent with emission from
220   aromatic organic compounds containing 1 or 2 fused aromatic rings and/or aromatic heterocycles
221   *(7-8,29)* (Fig. S7). Although assignment of fluorescence signatures to specific organic
222   compounds is non-specific, ~340 nm fluorescence is consistent with a base structure of 2-ring
223   aromatic organics like naphthalene, whereas ~275-285 nm fluorescence is more consistent with
224   1-ring aromatic organics like benzene *(8,29)*. The ~305 nm fluorescence may indicate either 1-
225   or 2-ring aromatics, depending on functional groups. We interpret ~305 nm and ~275 nm
226   fluorescence as organics that occurred with sulfates within the Bellegarde target (Fig. 4.D-F),
227   while we interpret ~285 nm fluorescence as organics that occurred with carbonate-phosphate-
228   amorphous silicate brown microcrystalline alteration zones within the Garde target (Fig. 2) *(8)*.
229   The ~340 nm fluorescence co-occurs with carbonate-phosphate-amorphous silicate alteration

230   zones in Garde but is not associated with particular phases in Guillaumes and Bellegarde *(8)*.
231   Both organics in phosphate-containing alteration zones and/or inorganic Ce-containing
232   phosphate can explain 340 nm fluorescence in Garde *(8)*. In Guillaumes and Bellegarde, 340 nm
233   fluorescence is predominantly uncoupled from phosphate detections, suggesting part of this
234   signal is best assigned to organics *(8)*. However, that some or all of the ~340 nm fluorescence
235   signal is from Ce cannot be excluded *(8)*.

236   When taken into context with Curiosity observations of organic material in mudstones *(21)*, this
237   study's confirmation of organic material in igneous rocks implies a diverse relationship between
238   geological processes and organic compounds on Mars. Several explanations for the presence of
239   Martian organics are possible, e.g., infall of meteoritic material *(6)*, *in situ* synthesis mechanisms
240   *(18-19,26)*, or a putative relic Martian biosphere. The association between organics and sulfate-,
241   phosphate-, perchlorate-, carbonate-, and amorphous silicate-bearing mineralogy as well as
242   alteration textures suggests that aqueous alteration of igneous rocks may have played a role in
243   the preservation or even synthesis of these particular organics, as seen for similar organics-
244   mineral correlations in Martian meteorites *(18-19,26)*. However, potentially organic, widespread
245   ~340 nm fluorescence could suggest other processes, such as dust, contributed to detections. We
246   note that some mineral phase associations may not be apparent due to instrument limitations *(8)*,
247   and higher spatial resolution analyses upon return of these samples to Earth are necessary to
248   conclusively establish the origins of the detected organics.

249

250   We did not detect Raman peaks consistent with aromatic organic compounds, such as the C=C
251   stretching mode (or G band) around ~1600 cm^{-1}. However, Raman scattered light is several
252   orders of magnitude weaker than fluorescence *(8,29)*. Organic concentrations were likely
253   insufficient to produce detectable Raman scattering, either due to low original concentration or
254   subsequent degradation. Conservative estimates of quantification suggest a range from 5×10^{-11}
255   to 3×10^{-10} grams of aromatic organics in localized points in the scan *(8)*. Estimates from the
256   average fluorescence maps suggest a bulk concentration of 0.1 to 10 ppm, with higher
257   concentrations associated with more aqueously altered surfaces *(8)*, consistent with known bulk
258   concentrations of organics, containing one and two ring aromatic species, indigenous to Martian
259   meteorites (11.2 ± 6.9 ppm *(18)*) and Curiosity rover detections in mudstones (~70 ppbw to 10.6
260   ± 8.9 ppm *(6,21)*). The SHERLOC observations cement these previous detections of Martian
261   organics *(18-19,21)* and reveal that the type, distribution, and material-associations are highly
262   complex and are vital to understand in order to determine evidence of potential past life and
263   provide key insights into the organic chemistry of terrestrial planets.
264
265   Collectively, the data show the six drilled samples collected by Perseverance are
266   astrobiologically significant. The evidence for carbonation, formation of sulfates and
267   perchlorates, and fluorescence signatures consistent with organics present within these materials
268   indicates an interplay between igneous rocks, aqueous alteration, and organic material on Mars.

Acknowledgements

References:

[1] K. A. Farley et al., Mars 2020 mission overview, *Space Sci. Rev* **216**, 1-41 (2020).

[2] T. A. Goudge et al., Assessing the mineralogy of the watershed and fan deposits of the Jezero crater paleolake system, Mars. *J. Geophys. Res. Planets* **120**, 775-808 (2015).

[3] B. L. Ehlmann et al., Orbital identification of carbonate-bearing rocks on Mars. *Science* **322**, 1828-1832 (2008).

[4] B. H. Horgan et al., The mineral diversity of Jezero crater: Evidence for possible lacustrine carbonates on Mars. *Icarus* **339**, 113526 (2020).

[5] R. Navarro-González et al., Reanalysis of the Viking results suggests perchlorate and organics at midlatitudes on Mars. *J. Geophys. Res. Planets* **115**, (E12) (2010).

[6] J. L. Eigenbrode et al., Organic matter preserved in 3-billion-year-old mudstones at Gale crater, Mars. *Science* **360**, 1096–1101 (2018).

307   [7] R. Bhartia et al., Perseverance's Scanning Habitable Environments with Raman and
308   Luminescence for Organics and Chemicals (SHERLOC) Investigation. *Space Sci. Rev.* **217**, 58
309   (2021).

310   [8] Materials and methods are available as supplementary materials.

311   [9] K. Farley et al., Aqueously-altered igneous and sedimentary rocks on the floor of Jezero
312   crater, Mars, *Science* **377**, eabo2196 (2022).

313   [10] Y. Liu et al., An olivine cumulate outcrop on the floor of Jezero crater, Mars, *Science* **377**,
314   1513-1519 (2022).

315   [11] M. M. Tice et al. Primary and Alteration Textures of Séítah Formation Rocks Inferred by X-
316   ray Fluorescence and Diffraction. *Sci. Adv.* (accepted).

317   [12] K. M. Stack et al., Photogeologic map of the perseverance rover field site in Jezero Crater
318   constructed by the Mars 2020 Science Team. *Space Sci. Rev.* **216**, 1-47 (2020).

319   [13] J. Razzell Hollis et al., A deep-ultraviolet Raman and Fluorescence spectral library of 62
320   minerals for the SHERLOC instrument onboard Mars 2020. *Planet. Space Sci.* **209**, 105356
321   (2021).

322   [14] J. Razzell Hollis et al., Deep-ultraviolet Raman spectra of Mars-relevant evaporite minerals
323   under 248.6 nm excitation. *Icarus* **357**, 114067 (2021).
324
325   [15] J. D. Tarnas, et al., Characteristics, origins, and biosignature preservation potential of
326   carbonate-bearing rocks within and outside of Jezero crater. *J. Geophys. Res. Planets* **126**,
327   e2021JE006898 (2021).
328
329   [16] E. L. Scheller et al., Formation of Magnesium Carbonates on Earth and Implications for
330   Mars. *J. Geophys. Res. Planets* **126**, e2021JE006828 (2021).
331
332   [17] V. F. Chevrier and M. Morisson, Carbonate-Phyllosilicate Parageneses and Environments of
333   Aqueous Alteration in Nili Fossae and Mars. *J. Geophys. Res. Planets* **126** (2021).
334
335   [18] A. Steele et al., The provenance, formation, and implications of reduced carbon phases in
336   Martian meteorites. *Meteorit. Planet. Sci.* **51**, 2203–2225 (2016).
337
338   [19] A. Steele et al., Organic synthesis associated with serpentinization and carbonation on early
339   Mars. *Science* **375**, 172-177(2022).
340

341 [20] R. V. Morris et al., Identification of carbonate-rich outcrops on Mars by the Spirit rover.
342 *Science* **329**, 421-424 (2010).

343

344 [21] C. Freissinet et al., Organic molecules in the Sheepbed Mudstone, Gale Crater, Mars. *J.*
345 *Geophys. Res.* **120**, 495-514 (2015).

346

347 [22] R. Hu et al., Tracing the fate of carbon and the atmospheric evolution of Mars. *Nature*
348 *communications* **6**, 1-9 (2015).

349

350 [23] M. H. Hecht et al., Detection of perchlorate and the soluble chemistry of martian soil at the
351 Phoenix lander site. *Science* **325***, 64-67 (2009).

352

353 [24] P. E. Martin, P. E et al., Reevaluation of perchlorate in Gale crater rocks suggests
354 geologically recent perchlorate addition. *J. Geophys. Res. Planets* **125**, e2019JE006156 (2020).

355

356 [25] E. K. Leask et al., Challenges in the search for perchlorate and other hydrated minerals with
357 2.1-μm absorptions on Mars. *GRL* **45**, 12-180 (2018).

358

359 [26] A. Steele et al., Organic synthesis on Mars by electrochemical reduction of CO_2. *Science*
360 *Advances* **4**, eaat5118 (2018).

361

362 [27] B. L. Carrier & S. P, Kounaves, The origins of perchlorate in the Martian soil. *GRL* **42**,
363 3739-3745 (2015).

364

365 [28] D. C. Catling et al., Atmospheric origins of perchlorate on Mars and in the Atacama. *J.*
366 *Geophys. Res. Planets* **115**, E1 (2010).

367

368 [29] R. Bhartia et al., Classification of organic and biological materials with deep
369 ultraviolet excitation. *Appl. Spectrosc.* **62**, 1070–1077 (2008).

370

371 *Supplementary references*

372 [30] Fries, M. D., et al. "The SHERLOC Calibration Target on the Mars 2020 Perseverance
373 Rover: Design, Operations, Outreach, and Future Human Exploration Functions." *Space Science*
374 *Reviews* **218**, 1-33 (2022).

375 [31] K. Uckert et al., A semi-autonomous method to detect cosmic rays in Raman hyperspectral
376 data sets. *Applied Spectroscopy* **73**, 1019-1027 (2019).

377

378 [32] M. Newville et al., LMFIT: Non-Linear Least-Square Minimization and Curve-Fitting for
379 Python. Zenodo. 10.5281/zenodo.11813 (2014).

380

381   [33] P. Virtanen et al., SciPy 1.0: Fundamental Algorithms for Scientific Computing in Python.
382   *Nature Methods* **17**, 261-272 (2020).

383   [34] J. Razzell Hollis, D. Rheingold, R. Bhartia, L. W. Beegle, An Optical Model for
384   Quantitative Raman Microspectroscopy. *Appl. Spectrosc.* **74**, 684–700 (2020).

385   [35] B. L. Carrier et al., Attenuation of Ultraviolet Radiation in Rocks and Minerals:
386   Implications for Mars Science. *J. Geophys. Res. Planets*. **124**, 2599–2612 (2019).

387   [36] K. E. Kuebler et al., Extracting olivine (Fo–Fa) compositions from Raman spectral peak
388   positions. *GCA* 70, 6201-6222 (2006).
389
390   [37] M. Veneranda et al., Spectroscopic study of olivine-bearing rocks and its relevance to the
391   ExoMars rover mission. *Spec. Act. Part A: Molecular and Biomolecular Spectroscopy 223*,
392   117360
393
394   [38] K. S. Edgett, Perseverance's SHERLOC WATSON – post-landing refinement of relations
395   between focus, range, and image scale using images acquired on Mars, plus an update on
396   particulates on the detector. Zenodo. 10.5281/zenodo.5555292 (2021).
397
398   [39] S. Leutenegger et al., BRISK: Binary Robust invariant scalable keypoints," *2011*
399   *International Conference on Computer Vision*, pp. 2548-2555 (2011)
400
401   [40] G. Bradski (2000). The OpenCV Library. *Journal of Software Tools*. (2000).
402
403   [41] Z. Wu, Z. et al., Spectroscopic study of perchlorates and other oxygen chlorides in a
404   Martian environmental chamber. *EPSL* **452**, 123-132 (2016).
405
406   [42] J. D. Stopar et al., Raman efficiencies of natural rocks and minerals: Performance of a
407   remote Raman system for planetary exploration at a distance of 10 meters. *Spec. Act. Part A:*
408   *Molecular and Biomolecular Spectroscopy* **61**, 2315-2323 (2005).
409
410   [43] M. R. Salvatore et al., Bulk mineralogy of the NE Syrtis and Jezero crater regions of Mars
411   derived through thermal infrared spectral analyses. *Icarus* **301**, 76-96 (2018).
412
413   [44] R. J. Smith et al., X-Ray Amorphous Components in Sedimentary Rocks of Gale Crater,
414   Mars: Evidence for Ancient Formation and Long-Lived Aqueous Activity. *J. Geophys. Res.*
415   *Planets* **126**, e2020JE006782 (2021).
416
417   [45] E. Eshelman et al., Time-resolved detection of aromatic compounds on planetary surfaces
418   by ultraviolet laser induced fluorescence and Raman spectroscopy. *Planetary and Space Science*.
419   **119,** 200-207 (2015).
420
421   [46] E. Eshelman et al., Detecting aromatic compounds on planetary surfaces using ultraviolet
422   time-resolved fluorescence spectroscopy. *Planetary and Space Science* **151,** 1-10 (2018).
423

[47] E. Lalla et al., Combined spectroscopic analysis of terrestrial analogs from a simulated astronaut mission using the laser-induced breakdown spectroscopy (LIBS) Raman sensor: implications for Mars. *App. Spec.* **75**, 1093-1113 (2021).

[48] S. Shkolyar et al., Detecting Kerogen as a Biosignature Using Colocated UV Time-Gated Raman and Fluorescence Spectroscopy. *Astrobiology* **18**, 431–454 (2018).

[49] S. Shkolyar et al., Detecting Ce^{3+} as a biosignature mimicker using UV time-resolved laser-induced fluorescence and Raman spectroscopy: Implications for planetary missions. *Icarus* **354**, 114093 (2021).

[50] M. Gaft et al., Modern luminescence spectroscopy of minerals and materials. Springer (2015).

[51] M. R. Baril and D. J. Huntley, Optal excitation spectra of trapped electrons in irradiated feldspars. *Journal of Physics: Condensed Matter* **15**, 8011 (2003).

[52] K. Sudarsanan and R.A. Young, Significant precision in crystal structural details - Holly Springs hydroxyapatite. *Acta Crystallographica Section B-Structural Crystallography and Crystal Chemistry* **B25**, 1534 (1969).

[53] D. J. Lieftink et al., The behavior of rare-earth elements in high-temperature Cl-bearing aqueous fluids - results from the Odegardens-Verk natural laboratory. *Canadian Mineralogist* **34**, 149-158 (1994).

[54] F. M. McCubbin et al., Hydrous melting of the martian mantle produced both depleted and enriched shergottites. *Geology* **40**, 683-686 (2012).

[55] S. L. Nadeau et al., Hydrogen and carbon abundances and isotopic ratios in apatite from alkaline intrusive complexes, with a focus on carbonatites. *GCA* **63**, 1837-1851 (1999).

[56] R. Bhartia et al., Explosives Detection and Analysis by Fusing Deep Ultraviolet Native Fluorescence and Resonance Raman Spectroscopy. in Laser-Based Optical Detection of Explosives (eds. Pellegrino, P. M., Holthoff, E. L. & Farrell, M. E.) 67–97 (Taylor & Francis Group, 2015).

[57] M. Suto et al., Quantitative photoabsorption and fluorescence spectroscopy of benzene, naphthalene, and some derivatives at 106–295 nm. *Journal of Quantitative Spectroscopy and Radiative Transfer* **48**, 79–89 (1992).

[58] L. W. Beegle, R. Bhartia, Mars 2020 SHERLOC Bundle, Planetary Data System (2021); https://doi.org/10.17189/1522643.

[59] E. L. Scheller, Laboratory datasets - Raman spectra. Zenodo (2022); https://doi.org/10.5281/zenodo.7212486.

470 [60] USGS, Mars 2020 Terrain Relative Navigation HiRISE Orthorectified Image Mosaic
471 (2020); https://doi.org/10.5066/P9QJDP48.
472
473 [61] J. F. Bell, J. N. Maki, Mars 2020 Mast Camera Zoom Data Bundle, from Operations Team,
474 calibrated products, Planetary Data System (2021); https://doi.org/10.17189/bs6b-4782.
475
476 [62] J. N. Maki, Mars 2020 Engineering Camera (ECAM) Bundles, Planetary Data System
477 (2021); https://doi.org/10.17189/1522847.
478
479 [63] A. C. Allwood, J. A. Hurowitz, Mars 2020 PIXL Raw and Processed Data Bundle,
480 Planetary Data System (2021); https://doi.org/10.17189/1522645.
481
482 Supplementary Materials:
483 Materials and Methods
484 Figs. S1 to S23
485 Table S1
486 References 30-63
487
488

Fig. 1: Rover images of the three abraded targets and their orbital context. (A) Map of orbitally defined geological units within Jezero crater from *(12)*, including the Crater Floor Fractured Rough unit (CF-fr) equivalent to the Máaz Fm and the Crater Floor Fractured 1 (CF-f1) unit equivalent to the Séítah Fm. Star shows the landing site, while white circles show the position of the three abraded targets. The locations of panels B and C are outlined in black rectangles. (B) Orbital infrared spectroscopy map showing the location of pyroxene- or olivine-bearing materials in the study area from *(4)*. Labels on white circles correspond to panel G. (C) HiRISE view of study area. (D) Mastcam-Z image showing the Garde patch on the Bastide outcrop. (E) Hazcam image showing the Bellegarde patch on the Rochette rock. (F) Navcam image showing the Guillaumes patch on the Roubion outcrop. (G) WATSON images of abraded targets analyzed in this study. Greyscale images for the colorblind are available in Fig. S9-S11 *(8)*.

Fig. 2: SHERLOC Raman and fluorescence results for the Garde abraded patch. (A) WATSON image. (B) Context image and scan outlines. (C-G) Grey-scale version of context image with data superimposed. (C) Fluorescence map showing the intensity of three main features centralized at 340 nm, 305 nm, and 285 nm in red, green, and blue respectively. (D) Raman mineral maps showing the location of detected olivine, carbonate, phosphate, and weak amorphous silicate features. White numbers as well as purple and green region of interest outlines (ROIs 1-2) were used for spectra shown in panel H. (E) Zoom in on panel B shows fluorescence correlation with intergranular spaces (outlined in white lines). (F) Fluorescence map from detail scan. (G) Raman map from detail scan and ROI 3-4 outlines intergranular and mineral domain textures (same legend as panel D) used in panel H. (H) Average ROI and single point (1-2) SHERLOC spectra (positions in panel D and G) compared with laboratory measurements. Greyscale images for the colorblind are available in Fig. S12-S15 *(8)*.

Fig. 3: SHERLOC Raman and fluorescence results for the Guillaumes abraded patch. (A) WATSON image. Two SHERLOC scans (yellow outlines) and one PIXL scan (black outline) shown.(B) Context image and scan outlines. (C) Average Raman spectrum compared with laboratory measurements of amorphous silicate, Na-perchlorate, and anhydrite. Laboratory spectral features at 1500-1600 cm^{-1} are O_2 (vertical, dotted line) and organic contaminants. (D-F) Grey-scale version of context image with data superposed. (D) Fluorescence map showing the intensity of three main features centralized at 340 nm, 305 nm, and 275 nm in red, green, and blue respectively. White circles indicate locations exposed to LIBS shots *(8)*. (E-F) Low and high SNR [8] Raman mineral maps showing the locations of detected perchlorate, Ca-sulfate with and without hydration, and 965 cm^{-1} peaks. (G) Raman spectra (positions indicated with numbers in panel E-F) from SHERLOC (1-4) compared with laboratory measurements. Greyscale images for the colorblind are available in Fig. S16-S19 *(8)*.

Fig. 4: SHERLOC Raman and fluorescence results for the Bellegarde abraded patch. (A) WATSON image. (B) Context image and scan outlines (C) Average Raman spectrum compared with laboratory measurements of amorphous silicate and obsidian. Laboratory spectral features at 1500-1600 cm^{-1} are O_2 (vertical, dotted line) and trace organic contaminants. (D-F) Grey-scale version of context image with data superposed. (D) Fluorescence map showing the intensity of three main features centralized at 340 nm, 305 nm, and 275 nm in red, green, and blue respectively. (E-F) Low and high SNR *(8)* Raman mineral maps showing the location of detected Ca-sulfate with and without hydration, carbonate, and 975 cm^{-1} peaks. (G) Raman spectra (positions indicated with numbers in panel E-F) from SHERLOC (1-3) compared with laboratory measurements (full hydrated sulfate spectrum in Fig. S3 *(8)*). Greyscale images for the colorblind are available in Fig. S20-S23 *(8)*.

Science
AAAS

Supplementary Materials for

Aqueous alteration processes and implications for organic geochemistry in Jezero crater, Mars

Eva L. Scheller & Joseph Razzell Hollis, Emily L. Cardarelli, Andrew Steele, Luther W. Beegle, Rohit Bhartia, Pamela Conrad, Kyle Uckert, Sunanda Sharma, Bethany L. Ehlmann, William J. Abbey, Sanford A. Asher, Kathleen C. Benison, Eve L. Berger, Olivier Beyssac, Benjamin L. Bleefeld, Tanja Bosak, Adrian J. Brown, Aaron S. Burton, Sergei V. Bykov, Ed Cloutis, Alberto G. Fairén, Lauren DeFlores, Kenneth A. Farley, Deidra M. Fey, Teresa Fornaro, Allison C. Fox, Marc Fries, Keyron Hickman-Lewis, William F. Hug, Joshua E. Huggett, Samara Imbeah, Ryan S. Jakubek, Linda C. Kah, Peter Kelemen, Megan R. Kennedy, Tanya Kizovski, Carina Lee, Yang Liu, Lucia Mandon, Francis M. McCubbin, Kelsey R. Moore, Brian E. Nixon, Jorge I. Núñez, Carolina Rodriguez Sanchez-Vahamonde, Ryan D. Roppel, Mitchell Schulte, Mark A. Sephton, Shiv K. Sharma, Sandra Siljeström, Svetlana Shkolyar, David L. Shuster, Justin I. Simon, Rebecca J. Smith, Kathryn M. Stack, Kim Steadman, Benjamin P. Weiss, Alyssa Werynski, Amy J. Williams, Roger C. Wiens, Kenneth H. Williford, Kathrine Winchell, Brittan Wogsland, Anastasia Yanchilina, Rachel Yingling, and Maria-Paz Zorzano

Correspondence to: eschelle@mit.edu

This PDF file includes:

Materials and Methods
Figs. S1 to S23
Table S1
References 30-63

Materials and Methods

S1. SHERLOC operation

SHERLOC is a deep-ultraviolet Raman and fluorescence spectrometer *(29)* mounted on the turret at the end of *Perseverance*'s robotic arm, alongside a high-resolution camera named WATSON (Wide-Angle Topographic Sensor for Operations and eNgineering) *(7)*. SHERLOC operates by scanning the target surface with a 110 μm diameter, 248.5794 nm pulsed laser, collecting any back-scattered Raman scattering and fluorescence emissions produced by illuminated material in the near-subsurface, which are detected by a 512x2048 pixel e2v 42-10 CCD kept at –28 ºC by a phase change material. The laser spot is moved from point to point in a grid by an internal scanning mirror, acquiring a combined Raman and fluorescence spectrum for each point. Spectra are measured between 250 and 354 nm, at a spectral resolution of 0.269 nm ($\sim$40 cm^{-1} in the Raman region) and 0.071 nm/pixel ($\sim$10 cm^{-1}/pixel). By using deep-ultraviolet excitation, the Raman spectrum is compressed into a narrow spectral range (250–275 nm) that is relatively free of fluorescence signal, allowing for spectral separation of the two phenomena in a single measurement. SHERLOC scans can be up to 1296 points, and cover an area of up to 7x7 mm. The hollow cathode NeCu laser spot is annular in shape, with an outer diameter of $\sim$110 μm, and is fired in 40 μsecond pulses at 80 Hz, with an estimated pulse energy of $\sim$9 μJ at the start of mission. The instrument has a working distance of 48 mm, and focusing is achieved using an autofocus context imager (ACI), which also acquires a high-resolution, grayscale image of the target surface at $\sim$10.1 μm/pixel. SHERLOC typically operates after local sunset, to maximize the time that the phase change material (PCM) can maintain the detector's ideal operating temperature of −28 ºC *(7)*.

Arm placement accuracy

Based on pre-launch assessments of arm placement accuracy under terrestrial gravity, *Perseverance*'s robotic arm is capable of placing SHERLOC within 12 mm of a targeted location. Lateral arm drift during operation is expected to be <100 μm/min *(7)*. The SHERLOC scanning mirror itself has a positioning error of <22 μm at the target.

Spectral calibration, resolution and accuracy

The SHERLOC spectral calibration during surface operations on Mars has an estimated uncertainty of ±5 cm^{-1} (±0.004 nm) in the 700–1800 cm^{-1} region (253.0–260.2 nm). The uncertainty was estimated by analyzing observed Raman peak positions for the ten SHERLOC calibration target materials mounted to the front of the rover, which were measured on sols 59 and 181, and comparing them to pre-launch values obtained on a laboratory instrument *(30)*. This comparison was done to evaluate any potential changes in calibration that may have occurred during launch, cruise, or landing, and determined that a small linear correction was needed, as described by *(30)*. The stated spectral uncertainty reflects the updated calibration, which was applied to all spectra reported in this article.

Once selected, each target presented here was abraded by *Perseverance*'s abrasion tool prior to characterization by SHERLOC *(1)*. The abraded patch is circular, approximately 45 mm in diameter, and 8–10 mm deep (Fig. 1). The abraded patch was then cleaned of dust/tailings using a jet of compressed gas from the gas Dust Removal Tool (gDRT), providing a clean, flat rock surface for proximity science analysis *(1)*. SHERLOC operates by scanning the target surface in a grid in order to construct Raman mineral and fluorescence maps, and analyses generate three different types of scans, referred to as survey (coverage: 5x5 mm, resolution: 140 µm), high-dynamic range (HDR) (coverage: 7x7 mm, resolution: 740 µm), and detail scans (coverage: 1x1 mm, resolution: 100 µm). In addition, survey scans are shot with 15 pulses per point (ppp), HDR scans are shot with between 250-500 ppp, and detail scans are shot with 500 ppp. This means survey scans will have low SNR Raman spectra compared with Raman spectra from HDR and detail scans. Hence, fluorescence and low SNR Raman mineral maps in Fig. 3-4 were created from survey scan results. High SNR Raman mineral maps were created from HDR scans in Fig. 2-4. Both fluorescence detail and Raman detail maps were created from detail scans in Fig. 2. Further detail for the scans performed on each target can be read below.

Guillaumes: The Guillaumes abraded target was characterized over sols 161–162. On sol 161, SHERLOC conducted one survey scan of 36x36 points in a 5x5 mm area at 15 pulses per point (ppp), and three co-located high dynamic range (HDR) scans of 10x10 points in a 7x7 mm area at 100, 100, and 300 ppp respectively. On sol 162, SHERLOC was positioned over a second area of the abraded target (Fig. 3) and conducted one survey scan of 36x36 points in a 5x5 mm area at 15 ppp and two co-located HDR scans of 10x10 points in a 7x7 mm area, both at 250 ppp. The results of the sol 162 survey and HDR #2 scans are shown in Fig. 3.

Bellegarde: The Bellegarde abraded target was characterized on sol 186 using one survey scan of 36x36 points in a 5x5 mm area at 15 ppp, and two HDR scans of 10x10 points in a 7x7 mm area, both at 250 ppp. The results of the survey and HDR #2 scans are shown in Fig. 4.

Garde: The Garde abraded target was characterized over sols 207–208. On sol 207, SHERLOC conducted one survey scan of 36x36 points in a 5x5 mm area at 15 ppp, and two HDR scans of 10x10 points in a 7x7 mm area, both at 500 ppp. On Sol 208, SHERLOC conducted three detail scans of 10x10 points in three different 1x1 mm areas that overlapped with the survey area, all at 500 ppp. The results of the fluorescence survey, HDR #2 scans, and the central detail scan are shown in Fig. 2.

S2. Spectral Processing
Due to the curved projection of the DUV spectrum onto SHERLOC's detector, the SCCD is divided into three vertical binning regions that are read out separately in order to minimize noise. For each region in each spectrum, an active frame is acquired while the laser is firing and a dark frame is acquired with the same duration without triggering the laser, which is then subtracted from the active frame. The full 250–354 nm spectrum can be obtained by recombining the three

regions, but this introduces additional noise in the Raman region that may obscure weak Raman signals. To avoid this when generating Raman data products, Region 1 (250–284 nm) is processed separately without recombination. Large positive (active frame) and negative (dark frame) spikes in the spectral data that were typically <3 pixels wide were due to cosmic rays impacting the detector during an acquisition.

Initial data processing was done using NASA internal software produced at the Jet Propulsion Laboratory by K. Uckert, named Loupe. Full processing includes dark frame subtraction, normalization to measured laser output, and cosmic ray removal using the method described in *(31)*. Loupe also provides functionality for correlating individual spectra to specific points on the ACI image based on scanning mirror positioning. Further data processing was done using custom Python scripts, following methods described in *(13)*. This includes polynomial baseline subtraction, automatic peak detection, and determining peak positions via Gaussian fitting. The requirements for automatic peak detection are local maxima that are at least 50 cm^{-1} apart, >5% of the spectrum's maximum intensity (after baseline subtraction), and >2 times the background noise (estimated as the standard deviation of baselined intensity in the peak-free region between 2000 and 2100 cm^{-1}). Furthermore, peak identification was also performed semi-quantitatively and subsequently compared to automated detections. Semi-quantitative detections were performed by identifying peaks with intensity >2 times the noise and a full-width half maximum that is >3 pixels (> ~30 cm^{-1}) wide. In all cases, peak fitting was performed by assigning a Gaussian function to each peak, and freely fitting the sum Gaussian curve to the data via either linear least square regression using the LMFIT python package *(32)* or the Levenberg-Marquardt method using the Scipy python package *(33)*.

Mineral identification
Mineralogical assignments were done by comparing baselined SHERLOC spectra and fitted peak positions to the SHERLOC spectral library, a database of spectral standards for minerals and organic compounds measured on Earth using the Brassboard instrument, an optical analog of the SHERLOC flight model that was adapted to function under terrestrial ambient conditions *(13)*. The mineral standard spectra shown in Figs. 2-4 are taken from the database and described in detail by *(13)* with the exception of perchlorate spectra obtained later, which are detailed below. Following mineral identification of each automated and semi-quantitatively defined peak through above-described methods, we constructed mineral maps of each obtained grid point within Figs. 2-4. Deriving quantitative concentrations of minerals from the Raman spectra is not currently possible *(34)*. Details outlining different Mars-relevant minerals and rocks ability to attenuate UV radiation and thus the SHERLOC DUV laser are detailed in *(35)*. As different minerals have different Raman scattering cross sections and peak intensities, not all points scanned exhibit peaks above the level of detection for a mineral phase, and will therefore appear unclassified.

Raman and fluorescence intensity maps

Spectral intensity maps of both Raman and fluorescence spectra were generated using three pre-defined spectral bands, and assigning the summed intensities of each band in each spectrum to the R, G, B values of the corresponding pixel, normalized to the 2% and 98% percentiles for all three bands across the entire map. For fluorescence maps, R, G, B values represent the 330–350 nm, 295–315 nm, and 265–285 nm bands, respectively, of the full composition spectrum; for Raman maps, R, G, B values represent the 1075–1125 cm^{-1}, 995–1045 cm^{-1}, and 945–995 cm^{-1} bands of the baselined Region 1 spectrum. The Raman spectral intensity maps were compared to the mineral identification maps for secondary validation, and the resulting product is the presented mineral maps in Figs. 2-4.

Olivine doublet peak convolution

SHERLOC detection of olivine in Garde was based on the appearance of a single Raman peak at 820–840 cm^{-1}, rather than the doublet at ~820 and ~850 cm^{-1} that has been widely reported for olivines in the literature *(36-37)*. The convolution of the olivine doublet into a single peak was also observed in laboratory measurements of olivines using the Brassboard, SHERLOC's terrestrial analog instrument, and is due to the 40–50 cm^{-1} spectral resolution of both instruments, as described in *(13)*. It may still be possible to quantitatively derive olivine Fo# compositions from the convoluted peak position, based on the shifting doublet positions reported in *(36-37)*, but current analysis is limited to qualitatively associating lower Raman shifts to lower Fo#.

S3. Image processing

SHERLOC includes two imaging subsystems, each equipped with a CCD camera: the Wide Angle Topographic Sensor for Operations and eNgineering (WATSON) and the Autofocus Context Imager (ACI) *(7,38)*. WATSON provides color imaging (1600 x 1200-pixel) of analysis targets from 2.5-40cm standoff distances. WATSON is able to contextualize the SHERLOC and PIXL instrument data, acquire stand-alone observations of rock surfaces, and image rover components and calibration targets to maintain the instruments onboard. The ACI acquires high-resolution grayscale images (1600 x 1200-pixel, ~10.1 µm/pixel spatial scale) at a working distance of 4.5-5 cm to focus SHERLOC's laser and provide context for spectroscopic measurements *(7)*. Both of these imaging subsystems' camera heads are mounted atop a rotatable turret on the robotic arm of the Perseverance rover, and can be independently positioned on a chosen target to provide complementary information, though they are not co-boresighted *(7)*.

The ACI focus merge products used here were created on Earth and flat-fielded using "sky flat" images acquired by ACI of the Martian sky on Sol 77. ACI focus stacks consist of 31 images obtained at different focus positions that capture the scene in increments of ~0.2 mm focus range (e.g., 45.0 mm to 50.4 mm in 31 steps). Images outside the below ranges were not in focus and

thus not used in the creation of the focus merge products. The images used in each focus merge product were as follows:

Guillaumes_161 - sol 161 - images 16-26 of 31
Guillaumes_162 - sol 162 - images 13-31 of 31
Bellegarde_186 - sol 186 - images 15-20 of 31
Garde_207 - sol 207 - images 15-19 of 31
Dourbes_257 - sol 257 - images 14-21 of 31
Dourbes_269 - sol 269 - images 14-20 of 31

Image registration and processing was performed using a custom Python script that utilized corresponding ACI (non-focus merged) and WATSON (onboard focus merge) images for a target to create an overlay. Keypoint detection was performed using the Binary Robust Invariant Scalable Keypoints (BRISK) method (39) and subsequently matched using the Fast Library for Approximate Nearest Neighbors (FLANN) based matcher utilizing the OpenCV python package (40). Colors from the two images were blended in hue, saturation, value (HSV) space to create a "colorized" ACI. Each colorized ACI was then overlaid with a map of laser points targeted by SHERLOC and generated in Loupe for each scan type (see S2).

S4. Assessment of carbonate and olivine compositions

The carbonate peak positions observed within interstitial materials and surrounding grains are observed to be within ± 5 cm^{-1} uncertainty of each other (Fig. 2.H). Laboratory data show that Mg-rich carbonates, such as dolomite and magnesite, have peak positions of 1095-1100 cm^{-1}, while Ca-rich and Fe-rich carbonates have peak positions at 1080-1087 cm^{-1} (13-14). Although some of our carbonate measurements fall within the uncertainty of these ranges, wavenumber peak positions mostly between them suggest solid solutions of either Fe-Mg or Ca-Mg carbonate, similar to carbonates in Martian meteorites (18-19). Other Perseverance instrument observations found mixed Fe- and Mg-carbonates consistent with SHERLOC observations (9,11). The position of the olivine peak appears shifted compared to our reference spectra, which were acquired for Mg-rich olivines with Fo# 80-90 (13); lower frequency indicates that the olivines present in Garde are relatively Fe-rich by comparison (10,36-37).

S5. Perchlorate laboratory measurements

The measurement of reference DUV Raman spectra for synthetic perchlorate salts was done using the SHERLOC brassboard instrument, an optical analog of the flight model that was designed to work under terrestrial ambient conditions (13). The salts and their sources were as follows: sodium perchlorate monohydrate (Sigma Aldrich 310514), potassium perchlorate (Alfa Aesar A11296), magnesium perchlorate (Sigma Aldrich 63102), and calcium perchlorate hydrate (Alfa Aesar 11655), all of which had reported purities of >95%. Each salt was characterized as a powder on a clean Aluminum wafer and all measurements were done under ambient conditions;

the calcium perchlorate hydrate deliquesced during measurement. Spectra were collected and processed using the method described in *(13)*.

S6. Assessment of perchlorate species

Detailed consideration of multiple different chemical compounds were considered for assignment of Guillaumes perchlorate spectra. Fig. S4 demonstrates several potential minerals that were assessed as an alternative to a perchlorate origin, including carbonate, phosphates, and sulfates. We compared our strongest SHERLOC spectra to a number of different perchlorate salts, including anhydrous and hydrated species, that were obtained through laboratory measurements with the SHERLOC Brassboard, an analog DUV Raman and fluorescence instrument at the NASA Jet Propulsion Laboratory with similar sensitivity and spectral resolution to SHERLOC. The position of the major 950–955 cm^{-1} peak observed on Mars places it between the observed major peak positions of Na-perchlorate and fluorapatite. However, the observation of two minor peaks at 1090–1095 cm^{-1} and 1150-1155 cm^{-1} are both consistent with Na-perchlorate rather than fluorapatite, which only has a single secondary mode at 1050 cm^{-1} (Fig. S4). Of the perchlorates we measured in the laboratory, only Na-perchlorate exhibits the two minor peaks we observe, the others exhibit a single minor peak at 1095–1115 cm^{-1}. Therefore, despite the ~5–10 cm^{-1} difference in major peak position compared to our Na-perchlorate reference, we are confident that we have observed Na-perchlorate on Mars. When comparing SHERLOC spectra to hydrous and anhydrous versions of Na-perchlorate from *(41)*, we find that there is no conclusive difference in match to minor peaks. However, the only spectral evidence we have for hydration (the O–H stretching mode around 3300 cm^{-1}) was observed in locations that exhibited sulfate peaks, indicating a hydrated sulfate species rather than a hydrated perchlorate species. Last, we compared our spectra to those obtained for other oxygen chloride and chlorate species by a previous study *(41)*. Higher oxidative states will systematically shift the peak position upwards and will also alter the position of minor peaks. No examined alternative Na oxygen chlorides or chlorate yielded a match with either major or minor peaks of the SHERLOC spectra. It is possible that – yet unexamined – down-shifting of peaks related to other cation oxygen chlorides or chlorates, such as Ca and Mg species, could explain the major 950–955 cm^{-1} peaks. However, these would not be able to explain the position and shape of the two minor peaks that appeared in our strongest spectra.

S7. Assessment of fluorescence correlation with SuperCam LIBS shots

The two bright ~275 nm spots in Guillaumes, which are co-located with previous LIBS shots, are likely fluorescence emission from 1-ring aromatics either created by the LIBS plasma, or exposed by ablation of surface material. Given that this was done on an already abraded surface, it seems unlikely that we are examining pristine 1-ring aromatics in the sub-surface, instead we suspect that we are seeing the 1-ring aromatics produced by LIBS-induced photochemical breakdown of MMC (macromolecular carbons) present within the rock. However, we cannot

currently rule out the possibility that LIBS-induced crystal defects within the exposed rock may be producing the observed luminescence.

S8. Comparison between SHERLOC mineral identifications and other instruments

SHERLOC Raman detections of sulfates within the Bellegarde target correlate directly with Ca-sulfate detections and minor Mg-sulfate components by the PIXL elemental maps, cementing the interpretation of secondary mm-scale Ca/Mg-sulfate crystals (Fig. S5). The PIXL elemental maps also reveal closely spaced Ca-sulfate and Na-Cl phases correlating with white, anhedral patches within the Guillaumes target, but the maps were not measured over the same area as the SHERLOC Raman map (Fig. S6). Lastly, SuperCam LIBS and Raman observations also confirm the presence of mixed Na-Mg-Cl phases, Na-perchlorate, and Ca/Mg-sulfates within partially overlapping measurements compared to SHERLOC in Guillaumes and Bellegarde *(9)*.

In the remaining measured spots that cover the primary texture within the Guillaumes and Bellegarde targets, we did not detect definitive mineral Raman peaks. However, the average spectra for each scan of Guillaumes and Bellegarde reveal the presence of a broad peak centered at 1060 cm^{-1} with a full width half maximum (FWHM) of 160 cm^{-1} and low intensity, consistent with amorphous silicate. This spectrum was similar to the single-point detection of amorphous silicate found within Garde. PIXL observations of Bellegarde and Guillaumes indicate primary phases consist of pyroxene, plagioclase, and olivine, which were not observed in the SHERLOC data (Fig. S5-S6) *(9)*. SHERLOC cannot report on the presence of plagioclases, as the dominant Raman peak of plagioclase (around 500 cm^{-1}) falls within the spectral range of SHERLOC's edge filter, which significantly attenuates signal below 700 cm^{-1} and makes peaks in this range harder to detect *(13)*. Fe-rich pyroxenes and olivines may not have been detected for a number of reasons, for example low abundance, crystallographic orientation, or attenuation of the DUV signal due to Fe or opaqueness *(13,35,42)*. Alternatively, some of these phases may also be significantly disordered giving rise to broader, weaker Raman peaks similar to amorphous silicate signatures. Modeling of orbital data from the Thermal Emission Spectrometer predicted ~24% and ~15% amorphous silicate components within the Máaz and Seitah formations *(43)*. The Curiosity rover also detected 15-70 wt% X-ray amorphous components within samples of sedimentary rocks in Gale crater, suggesting the presence of amorphous silicates may be a common phenomenon on Mars *(44)*. While the SHERLOC Raman detections of amorphous silicates at present cannot distinguish between the proposed origin as volcanic glass, impact glass, or aqueous alteration of previously crystalline silicate phases, the amorphous silicates within Gale crater have been found to be more consistent with aqueous alteration of previously crystalline silicate phases *(44)*.

S9. Fluorescence assignment and laboratory measurements of phosphates
SHERLOC is capable of detecting organic material via DUV fluorescence emission and Raman scattering, and is most sensitive to compounds containing 1- and 2-ring aromatic units and/or aromatic heterocycles, which typically fluoresce within SHERLOC's spectral range *(29,45-47)*

(Fig. S7). Aromatic organic compounds typically dominate SHERLOC spectra, due to strong fluorescence emission and molecular resonance enhancement of Raman scattering (29,45-47) (Fig. S7). The only currently known inorganic material that causes fluorescence at the wavelengths relevant to the SHERLOC instrument is Ce (48-51). All other known inorganic materials in context with the measured mineralogy fluoresce at wavelengths higher than 350 nm (47,50). Hence, fluorescence signals centered at 275 nm, 285 nm, and 305 nm within the Bellegarde and Garde targets can be assigned to aromatic organic compounds with no interference from rare earth element fluorescence.

Some inorganic complexes, specifically Ce-containing phosphates such a merrilite or apatite, are known to fluoresce with maxima between 340 and 350 nm (47,49-50) (Fig. S8). A series of laboratory experiments were conducted on the Analogue Complimentary Raman for Operations oN Mars (ACRONM) SHERLOC analogue instrument at NASA Johnson Space Center. The ACRONM instrument build was modeled after the MOBIUS instrument, described in (13). Incident excitation is produced using a PhotonSystems NeCu70-248 hollow cathode laser producing 248.5794 nm excitation with a ~100 μm beam spot. The Raman scattered light is dispersed using a Horiba Scientific iHR 320 spectrometer equipped with a 300 g/mm grating. Fluorescence spectra of apatites with measured Ce concentrations (Table S1) were collected using a 20 Hz laser pulse rate with a 40 μs pulse width and ~4.7 μJ/pulse laser energy at the sample. For collection of a single spectrum, we averaged 30 spectra collected at the same point on the sample, each with an accumulation time of 0.01 seconds. For each apatite sample in Table S1, ten single spectra were collected at different sample locations to account for any heterogeneity of the fluorescence signal. For all samples, the fluorescence band positions and shapes were consistent for all ten points. The ten spectra were averaged for each sample, producing a single fluorescence spectrum representative of each sample, which are presented in Figure S8. Spectra were baselined using a linear function. The average spectra were then used to extract the band parameters presented in Table S1. It can be observed that even 100 ppm of Ce present in phosphates can result in fluorescence features centered at 340-350 nm, which overlaps with the fluorescence signal of 2-ring aromatics such as naphthalene (Fig. S8). Notably, no fluorescence signals centered at 275 nm, 285 nm, and 305 nm occur within the phosphate samples.

Within Bellegarde, one peak at 975 cm^{-1}, designated as a possible phosphate detection, also exhibited a 340 nm fluorescence response. However, the 340 nm fluorescence signal was more widespread within this target and predominantly occurred without 975 cm^{-1} peaks. Furthermore, 975 cm^{-1} peaks were detected without the 340 nm fluorescence response. In Guillaumes, the 340 nm fluorescence did not correlate with any particular mineral phase, occurred throughout the target, and phosphate-designated 965 cm^{-1} peaks occurred without the presence of 340 nm fluorescence. Fluorescence signals are stronger in intensity than Raman detections. Hence, it could be possible that 340 nm fluorescence from Ce-containing phosphate is detected, while the Raman signature of phosphates are not. It is also possible that other Ce-containing phases could

cause 340 nm fluorescence. However, we note that in general Ce-concentrations in phosphates are higher compared to those in other phases known to be present in the target, as Ce preferentially substitutes into phosphates. All of the laboratory measurements of other relevant phases for the Martian targets performed to this date on SHERLOC analogue instruments *(e.g. 13-14)* did not exhibit fluorescence signatures, except for the mentioned phosphates. As such, it is expected that phosphate would be the prime producer of Ce-associated 340 nm fluorescence. Several phosphate-designated 965-975 cm^{-1} peaks occurred in both Bellegarde and Guillaumes targets without the presence of 340 nm fluorescence, suggesting that these materials did not produce an inorganic 340 nm fluorescence peak related to their Ce-content. While Ce-containing phosphate may explain part of the 340 nm fluorescence signatures in Bellegarde, the 340 nm fluorescence is predominantly uncoupled to phosphate detections in both Bellegarde and Guillaumes. This suggests that part of 340 nm features are presently best explained as two ring aromatic compounds.

Within the Garde target, several measurement points, specifically within detail scans (Fig. 2.F-G), showed correlation between fluorescence signals centered at 340 and 285 nm and phosphate-designated Raman peaks positioned at 955-965 cm^{-1}. In this case, the intensity of the probable phosphate detections were observed to co-vary with the intensity of the 340 nm fluorescence as examined with a linear regression that resulted in R^2=0.95. However, we note that phosphate-designated 955-965 cm^{-1} detections within the scan of Fig. 2.D did not exhibit 340 nm fluorescence, similar to observations of Bellegarde and Guillaumes. Two hypotheses are possible for the origin of the phosphate and 340 nm fluorescence correlation in Garde. (1) 340 nm fluorescence is the result of Ce-bearing phosphate, which would explain the covarying intensity, while 285 nm fluorescence is the result of aromatic organics. (2) Aromatic organics that give rise to both 340 nm and 285 nm fluorescence preferentially occur within alteration/weathering zones that happen to be phosphate-containing. SHERLOC-WATSON characterized the 340 nm and 285 nm fluorescence features to occur in brown, microcrystalline interstitial zones affiliated with phosphate, carbonate, and amorphous silicates. Thus, these materials, including phosphates, appear to have been influenced by secondary alteration processes that occurred after protolith formation and were likely to preserve or even synthesize organic compounds.

S10. Quantification of organics

Fluorescence provides an exceptionally strong signal, enabling detection of fluorescent compounds even at very low concentrations *(7)*, while Raman is generally multiple orders of magnitude weaker than fluorescence but provides a spectrum highly specific to chemical structure, enabling identification of particular compounds. Measured Raman and fluorescence intensities are determined by laser energy at the target, the size of the illuminated volume within the target, the concentration and scattering cross-section/quantum yield of the organic molecule, and optical attenuation by surrounding material *(34)*. The presence of certain metals that have strong absorptions in the DUV, such as Fe *(35,42,48)* or Ce *(49)*, may attenuate measured signals from any organic molecules within the same sample. Because of such dependencies,

quantification of organic concentrations from either Raman or fluorescence signal yields is limited to estimations that utilize a set of assumptions and known instrument performance characteristics, and provide upper/lower bounds for concentration rather than specific values. To estimate the localized concentration and bulk concentrations observed, we utilized the optical performance model that was used to design and verify the performance of the SHERLOC instrument *(9,56)*. The model incorporates all the primary SHERLOC instrument parameters such as the laser energy at the target, the collection performance, the noise as a function of CCD operation temperature, CCD gain, background subtraction effects to noise, dark noise, and read noise to generate an expected analog to digital count for both signal and noise. This value is dependent on the interrogation volume, the quantum yield of the compound, and its concentration within the interrogation volume. The interrogation volume is approximated by the product of the illumination area and the depth of penetration. We assume that the instrument is focused (within ±500 μm of the optimal focus) and generates a 106 μm diameter annular beam *(34)*. The depth of penetration into a Mars simulate with similar Fe concentrations was shown to be up to 150 μm *(35)*. The current estimation in the model conservatively assumes a 75 μm depth of penetration. Using an average density of an igneous rock of 2.7 g/cm^3, the total mass analyzed in a single point measurement is 0.6 μg. Over a 1296 point map, this equates to a total mass of ~800 μg.

To determine the concentration of organics in a single point in the map, we use a highly conservative fluorescence cross-section for benzene (1.5 x 10^{-24} cm^2 sr^{-1} nm^{-1} molecule^{-1} *(57)*) at the SHERLOC excitation wavelength, 248.5794 nm. Based on these values, the model adjusts the concentration within a single spot to achieve the detected CCD counts (Fig. S7). The mass of organics is determined for a single point. To assess bulk concentration for comparison the average fluorescence spectrum of the map is used to determine the total mass of organics detected (Fig. S7). This is then divided by the total mass in the scanned volume to derive a concentration in terms of ppm. These values are used to bound the concentration for comparison to previous analyses on Mars and of Martian meteorites and provide a means to compare the difference as we traverse through Jezero crater.

S11. Data Sources
All SHERLOC spectral and WATSON image data used for this study is available through the NASA PDS SHERLOC data bundle *(58)*.

Reference spectra for perchlorates, phosphates, obsidian, and organic compounds used in Fig. 2-4, Fig. S4, Fig. S7, and Fig. S8 measured in the laboratory for this study are archived *(59)*. All other mineral laboratory spectra used in Fig. 2-4 and Fig. S4 are already published and available in *(13)*.

Below is additional information about how to find specific datasets used for each figure.

Fig. 1: HiRISE images are available in *(60)*.

Mastcam-Z images are available through the NASA PDS Mastcam-Z bundle *(61)*.

Image IDs for Garde image (panel D):

ZR0_0207_0685313671_348RAD_N0071836ZCAM08235_1100LMA01
ZR0_0207_0685313790_348RAD_N0071836ZCAM08235_1100LMA01
ZR0_0207_0685313812_348RAD_N0071836ZCAM08235_1100LMA01
ZR0_0207_0685313828_331RAD_N0071836ZCAM08235_1100LMA01
ZR0_0207_0685313855_348RAD_N0071836ZCAM08235_1100LMA01
ZR0_0207_0685313875_348RAD_N0071836ZCAM08235_1100LMA01
ZR0_0207_0685313904_348RAD_N0071836ZCAM08235_1100LMA01
ZR0_0207_0685313920_348RAD_N0071836ZCAM08235_1100LMA01
ZR0_0207_0685313949_348RAD_N0071836ZCAM08235_1100LMA01
ZR0_0207_0685313979_348RAD_N0071836ZCAM08235_1100LMA01
ZR0_0207_0685314010_332RAD_N0071836ZCAM08235_1100LMA01
ZR0_0207_0685314030_348RAD_N0071836ZCAM08235_1100LMA01
ZR0_0207_0685314057_398RAD_N0071836ZCAM08235_1100LMA01
ZR0_0207_0685314090_348RAD_N0071836ZCAM08235_1100LMA01
ZR0_0207_0685314124_332RAD_N0071836ZCAM08235_1100LMA01
ZR0_0207_0685314142_348RAD_N0071836ZCAM08235_1100LMA01
ZR0_0207_0685314170_348RAD_N0071836ZCAM08235_1100LMA01
ZR0_0207_0685314195_348RAD_N0071836ZCAM08235_1100LMA01
ZR0_0207_0685314224_348RAD_N0071836ZCAM08235_1100LMA01
ZR0_0207_0685314257_348RAD_N0071836ZCAM08235_1100LMA01
ZR0_0207_0685314288_348RAD_N0071836ZCAM08235_1100LMA01
ZR0_0207_0685314307_348RAD_N0071836ZCAM08235_1100LMA01
ZR0_0207_0685314369_348RAD_N0071836ZCAM08235_1100LMA01
ZR0_0207_0685314385_348RAD_N0071836ZCAM08235_1100LMA01
ZR0_0207_0685314415_348RAD_N0071836ZCAM08235_1100LMA01
ZR0_0207_0685314451_331RAD_N0071836ZCAM08235_1100LMA01
ZR0_0207_0685314488_331RAD_N0071836ZCAM08235_1100LMA01
ZR0_0207_0685314524_332RAD_N0071836ZCAM08235_1100LMA01
ZR0_0207_0685314543_348RAD_N0071836ZCAM08235_1100LMA01
ZR0_0207_0685314558_331RAD_N0071836ZCAM08235_1100LMA01
ZR0_0207_0685314586_348RAD_N0071836ZCAM08235_1100LMA01
ZR0_0207_0685314605_348RAD_N0071836ZCAM08235_1100LMA01
ZR0_0207_0685314634_348RAD_N0071836ZCAM08235_1100LMA01
ZR0_0207_0685314667_348RAD_N0071836ZCAM08235_1100LMA01
ZR0_0207_0685314687_348RAD_N0071836ZCAM08235_1100LMA01

ZR0_0207_0685314715_348RAD_N0071836ZCAM08235_1100LMA01
ZR0_0207_0685314734_348RAD_N0071836ZCAM08235_1100LMA01
ZR0_0207_0685314747_348RAD_N0071836ZCAM08235_1100LMA01
ZR0_0207_0685314764_348RAD_N0071836ZCAM08235_1100LMA01
ZR0_0207_0685314795_332RAD_N0071836ZCAM08235_1100LMA01
ZR0_0207_0685314861_389RAD_N0071836ZCAM08235_1100LMA01
ZR0_0207_0685314896_348RAD_N0071836ZCAM08235_1100LMA01
ZR0_0207_0685314930_348RAD_N0071836ZCAM08235_1100LMA01
ZR0_0207_0685314965_331RAD_N0071836ZCAM08235_1100LMA01
ZR0_0207_0685314997_348RAD_N0071836ZCAM08235_1100LMA01
ZR0_0207_0685314336_332RAD_N0071836ZCAM08235_1100LMA03
ZR0_0207_0685315029_348RAD_N0071836ZCAM08235_1100LMA01
ZR0_0207_0685315046_348RAD_N0071836ZCAM08235_1100LMA01
ZR0_0207_0685315072_331RAD_N0071836ZCAM08235_1100LMA01
ZR0_0207_0685315090_348RAD_N0071836ZCAM08235_1100LMA01
ZR0_0207_0685315104_389RAD_N0071836ZCAM08235_1100LMA01
ZR0_0207_0685315117_348RAD_N0071836ZCAM08235_1100LMA01
ZR0_0207_0685315132_348RAD_N0071836ZCAM08235_1100LMA01
ZR0_0207_0685315161_348RAD_N0071836ZCAM08235_1100LMA01
ZR0_0207_0685315193_348RAD_N0071836ZCAM08235_1100LMA01
ZR0_0207_0685315213_348RAD_N0071836ZCAM08235_1100LMA01
ZR0_0207_0685315227_331RAD_N0071836ZCAM08235_1100LMA01
ZR0_0207_0685315240_348RAD_N0071836ZCAM08235_1100LMA01
ZR0_0207_0685315254_348RAD_N0071836ZCAM08235_1100LMA01
ZR0_0207_0685315268_348RAD_N0071836ZCAM08235_1100LMA01
ZR0_0207_0685315298_348RAD_N0071836ZCAM08235_1100LMA01
ZR0_0207_0685315315_348RAD_N0071836ZCAM08235_1100LMA01
ZR0_0207_0685315343_348RAD_N0071836ZCAM08235_1100LMA01
ZR0_0207_0685315375_389RAD_N0071836ZCAM08235_1100LMA01
ZR0_0207_0685315394_348RAD_N0071836ZCAM08235_1100LMA01
ZR0_0207_0685315421_348RAD_N0071836ZCAM08235_1100LMA01
ZR0_0207_0685315441_348RAD_N0071836ZCAM08235_1100LMA01
ZR0_0207_0685315455_348RAD_N0071836ZCAM08235_1100LMA01
ZR0_0207_0685315487_348RAD_N0071836ZCAM08235_1100LMA01
ZR0_0207_0685315523_348RAD_N0071836ZCAM08235_1100LMA01
ZR0_0207_0685315556_331RAD_N0071836ZCAM08235_1100LMA01
ZR0_0207_0685315587_348RAD_N0071836ZCAM08235_1100LMA02
ZR0_0207_0685315604_348RAD_N0071836ZCAM08235_1100LMA01
ZR0_0207_0685315617_348RAD_N0071836ZCAM08235_1100LMA01
ZR0_0207_0685315632_348RAD_N0071836ZCAM08235_1100LMA01

ZR0_0207_0685315662_331RAD_N0071836ZCAM08235_1100LMA01
ZR0_0207_0685315681_331RAD_N0071836ZCAM08235_1100LMA01
ZR0_0207_0685315697_348RAD_N0071836ZCAM08235_1100LMA01
ZR0_0207_0685315726_331RAD_N0071836ZCAM08235_1100LMA01
ZR0_0207_0685315743_331RAD_N0071836ZCAM08235_1100LMA01
ZR0_0207_0685315771_348RAD_N0071836ZCAM08235_1100LMA01
ZR0_0207_0685315805_348RAD_N0071836ZCAM08235_1100LMA01
ZR0_0207_0685315822_331RAD_N0071836ZCAM08235_1100LMA01
ZR0_0207_0685315850_331RAD_N0071836ZCAM08235_1100LMA01
ZR0_0207_0685315867_331RAD_N0071836ZCAM08235_1100LMA01
ZR0_0207_0685315894_348RAD_N0071836ZCAM08235_1100LMA01
ZR0_0207_0685315913_348RAD_N0071836ZCAM08235_1100LMA01
ZR0_0207_0685315926_348RAD_N0071836ZCAM08235_1100LMA01
ZR0_0207_0685315952_331RAD_N0071836ZCAM08235_1100LMA01
ZR0_0207_0685315986_348RAD_N0071836ZCAM08235_1100LMA01
ZR0_0207_0685316020_348RAD_N0071836ZCAM08235_1100LMA01
ZR0_0207_0685316039_348RAD_N0071836ZCAM08235_1100LMA01
ZR0_0207_0685316053_348RAD_N0071836ZCAM08235_1100LMA01
ZR0_0207_0685316067_348RAD_N0071836ZCAM08235_1100LMA01
ZR0_0207_0685316095_348RAD_N0071836ZCAM08235_1100LMA01
ZR0_0207_0685316114_348RAD_N0071836ZCAM08235_1100LMA01
ZR0_0207_0685316128_348RAD_N0071836ZCAM08235_1100LMA01
ZR0_0207_0685316141_331RAD_N0071836ZCAM08235_1100LMA01
ZR0_0207_0685316170_332RAD_N0071836ZCAM08235_1100LMA01
ZR0_0207_0685316187_348RAD_N0071836ZCAM08235_1100LMA01
ZR0_0207_0685316252_348RAD_N0071836ZCAM08235_1100LMA02
ZR0_0207_0685316269_348RAD_N0071836ZCAM08235_1100LMA01
ZR0_0207_0685316297_348RAD_N0071836ZCAM08235_1100LMA02
ZR0_0207_0685316314_331RAD_N0071836ZCAM08235_1100LMA01
ZR0_0207_0685316330_331RAD_N0071836ZCAM08235_1100LMA02
ZR0_0207_0685316362_331RAD_N0071836ZCAM08235_1100LMA01
ZR0_0207_0685317098_348RAD_N0071836ZCAM08235_1100LMA01
ZR0_0207_0685317110_331RAD_N0071836ZCAM08235_1100LMA01
ZR0_0207_0685317122_331RAD_N0071836ZCAM08235_1100LMA01
ZR0_0207_0685317134_384RAD_N0071836ZCAM08235_1100LMA01
ZR0_0207_0685317146_348RAD_N0071836ZCAM08235_1100LMA01
ZR0_0207_0685317160_331RAD_N0071836ZCAM08235_1100LMA01
ZR0_0207_0685317172_348RAD_N0071836ZCAM08235_1100LMA01
ZR0_0207_0685317185_331RAD_N0071836ZCAM08235_1100LMA01
ZR0_0207_0685314829_348RAD_N0071836ZCAM08235_1100LMA04

ZR0_0207_0685316381_331RAD_N0071836ZCAM08235_1100LMA01
ZR0_0207_0685316393_348RAD_N0071836ZCAM08235_1100LMA01
ZR0_0207_0685316405_331RAD_N0071836ZCAM08235_1100LMA01
ZR0_0207_0685316433_348RAD_N0071836ZCAM08235_1100LMA01
ZR0_0207_0685316452_348RAD_N0071836ZCAM08235_1100LMA01
ZR0_0207_0685316466_348RAD_N0071836ZCAM08235_1100LMA01
ZR0_0207_0685316478_348RAD_N0071836ZCAM08235_1100LMA01
ZR0_0207_0685316491_348RAD_N0071836ZCAM08235_1100LMA01
ZR0_0207_0685316505_348RAD_N0071836ZCAM08235_1100LMA01
ZR0_0207_0685316519_348RAD_N0071836ZCAM08235_1100LMA01
ZR0_0207_0685316547_348RAD_N0071836ZCAM08235_1100LMA01
ZR0_0207_0685316564_348RAD_N0071836ZCAM08235_1100LMA01
ZR0_0207_0685316576_348RAD_N0071836ZCAM08235_1100LMA01
ZR0_0207_0685316589_331RAD_N0071836ZCAM08235_1100LMA01
ZR0_0207_0685316602_348RAD_N0071836ZCAM08235_1100LMA01
ZR0_0207_0685316616_348RAD_N0071836ZCAM08235_1100LMA01
ZR0_0207_0685316630_348RAD_N0071836ZCAM08235_1100LMA01
ZR0_0207_0685316656_331RAD_N0071836ZCAM08235_1100LMA01
ZR0_0207_0685316673_348RAD_N0071836ZCAM08235_1100LMA01
ZR0_0207_0685316687_331RAD_N0071836ZCAM08235_1100LMA01
ZR0_0207_0685316701_348RAD_N0071836ZCAM08235_1100LMA01
ZR0_0207_0685316713_348RAD_N0071836ZCAM08235_1100LMA01
ZR0_0207_0685316726_331RAD_N0071836ZCAM08235_1100LMA01
ZR0_0207_0685316738_348RAD_N0071836ZCAM08235_1100LMA01
ZR0_0207_0685316764_348RAD_N0071836ZCAM08235_1100LMA01
ZR0_0207_0685316781_348RAD_N0071836ZCAM08235_1100LMA01
ZR0_0207_0685316793_331RAD_N0071836ZCAM08235_1100LMA01
ZR0_0207_0685316805_348RAD_N0071836ZCAM08235_1100LMA01
ZR0_0207_0685316831_348RAD_N0071836ZCAM08235_1100LMA01
ZR0_0207_0685316848_348RAD_N0071836ZCAM08235_1100LMA01
ZR0_0207_0685316860_348RAD_N0071836ZCAM08235_1100LMA01
ZR0_0207_0685316886_348RAD_N0071836ZCAM08235_1100LMA01
ZR0_0207_0685316903_331RAD_N0071836ZCAM08235_1100LMA01
ZR0_0207_0685316915_348RAD_N0071836ZCAM08235_1100LMA01
ZR0_0207_0685316927_348RAD_N0071836ZCAM08235_1100LMA01
ZR0_0207_0685316953_348RAD_N0071836ZCAM08235_1100LMA01
ZR0_0207_0685316970_348RAD_N0071836ZCAM08235_1100LMA01
ZR0_0207_0685316983_331RAD_N0071836ZCAM08235_1100LMA01
ZR0_0207_0685317007_348RAD_N0071836ZCAM08235_1100LMA01
ZR0_0207_0685317021_331RAD_N0071836ZCAM08235_1100LMA01

ZR0_0207_0685317035_331RAD_N0071836ZCAM08235_1100LMA01
ZR0_0207_0685317050_348RAD_N0071836ZCAM08235_1100LMA01
ZR0_0207_0685317066_348RAD_N0071836ZCAM08235_1100LMA01
ZR0_0207_0685317083_331RAD_N0071836ZCAM08235_1100LMA01
ZR0_0207_0685316217_348RAD_N0071836ZCAM08235_1100LMA03

NavCam and Hazcam images are available through the NASA PDS ECAM bundle *(62)*.
Specific Hazcam image link for Bellegarde (panel E):
https://mars.nasa.gov/resources/26227/abrasion-patch-on-rochette/
Image ID for Guillaumes (panel F):
NRF_0160_0681144352_237ECM_N0060000NCAM00314_07_195J.IMG

WATSON images are available from SHERLOC data bundle, Mars 2020 SHERLOC WATSON
Data Collection *(58)*. WATSON image of the Garde target (same as Fig. 2A) can be found under
sol 206. WATSON image of the Bellegarde target can be found under sol 185. WATSON image
of the Guillaumes target can be found under sol 160.

Fig. 2: Spectroscopic data from SHERLOC data bundle *(58)*, Processed Spectroscopy data
collection, sol 207 and sol 208 (Garde). Image data from SHERLOC data bundle, Mars 2020
SHERLOC ACI Data Collection, sol 207 and 208. Colorized by using image data from
SHERLOC data bundle, Mars 2020 SHERLOC WATSON Data Collection, sol 206.

Fig. 3, Fig. S1, Fig. S4: SHERLOC data bundle *(58)*, Processed Spectroscopy data collection, sol
162 (Guillaumes). Image data from SHERLOC data bundle, Mars 2020 SHERLOC ACI Data
Collection, Mars 2020 SHERLOC ACI Data Collection, sol 162. Colorized by using image data
from Mars 2020 SHERLOC WATSON Data Collection, sol 160.

Fig. 4, Fig. S3: SHERLOC data bundle *(58)*, Processed Spectroscopy data collection, sol 186
(Bellegarde). Image data from SHERLOC data bundle, Mars 2020 SHERLOC ACI Data
Collection, sol 186. Colorized by using image data from Mars 2020 SHERLOC WATSON Data
Collection, sol 185.

Fig. S2, Fig. S5, Fig. S6: PIXL data sets are available through the NASA PDS PIXL bundle *(63)*.
Guillaumes and Bellegarde abrasion patch data are listed under Processed data collection, sols
167 and 187, respectively. SHERLOC Bellegarde datasets are the same as for Fig. 4.
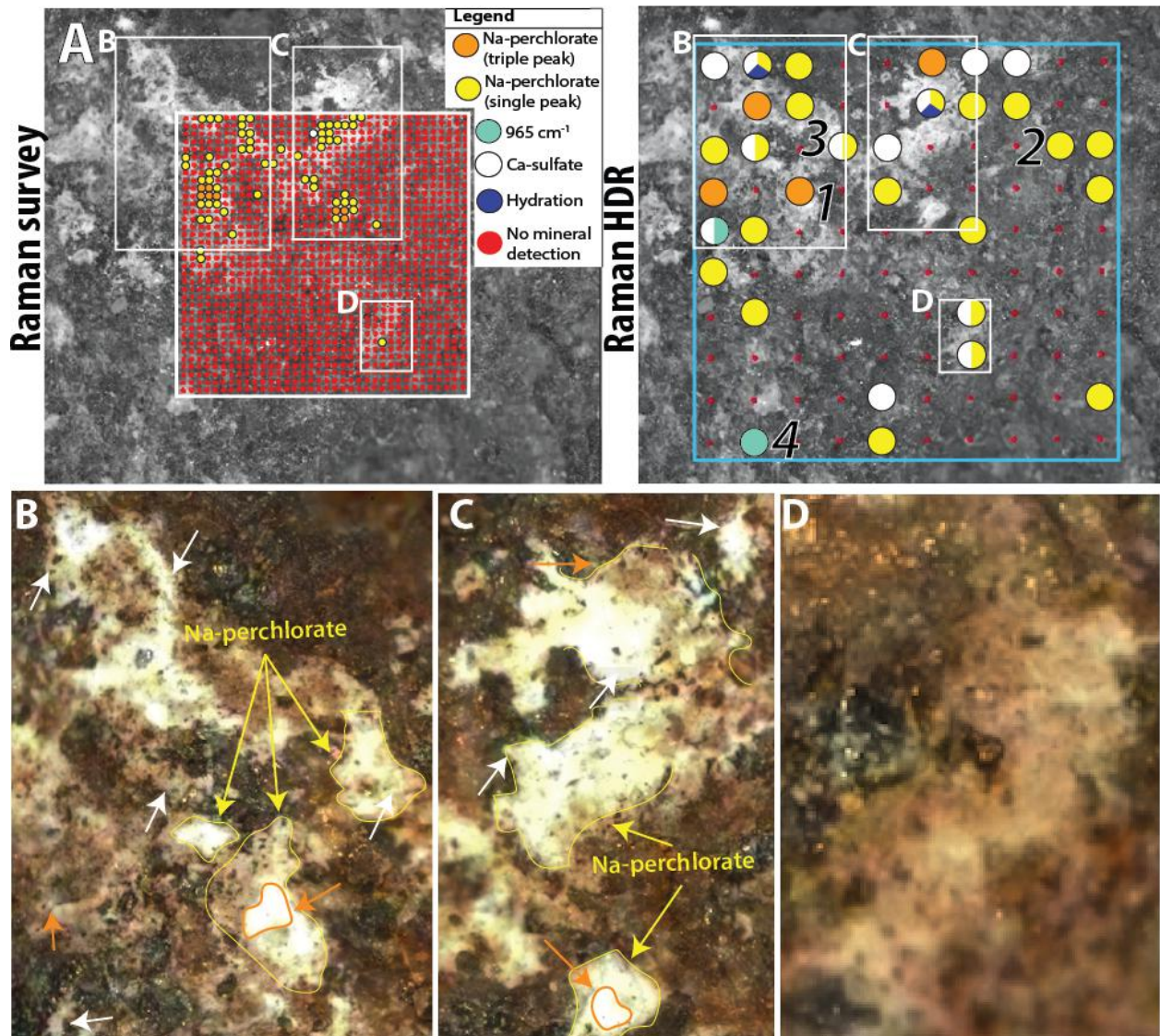
Fig. 7: Same datasets as in Fig. 2-4.

Fig. S1. SHERLOC context and WATSON image merge showing the textures of mineral assemblages within the Guillaumes target. (A) Mineral detections within survey and HDR scans of the Guillaumes target from Fig. 3. (B-D) Texture of high intensity Na-perchlorate detections (orange outline and arrows), low intensity less certain Na-perchlorate detections (yellow outlines and arrows) as well as occasional Ca-sulfate detections (white arrows). The mineral detections are mixed within anhedral, white, tan to reddish brown patches of material that are secondary to the primary lithology of the Guillaumes target.

Fig. S2. SHERLOC context and WATSON image merge showing the textures of mineral assemblages within the Bellegarde target. (A) Mineral detections within HDR scans of the Bellegarde target overlain on the PIXL elemental chemistry map of SO_3, MgO, and CaO from Fig. S5. (B-C) Texture of Ca-sulfate detections (white arrows). Ca-sulfates are detected within white anhedral to sub-euhedral crystals that have a reddish rim around them that appear secondary to the primary lithology. Textures of possible phosphate minerals are more nebulous.
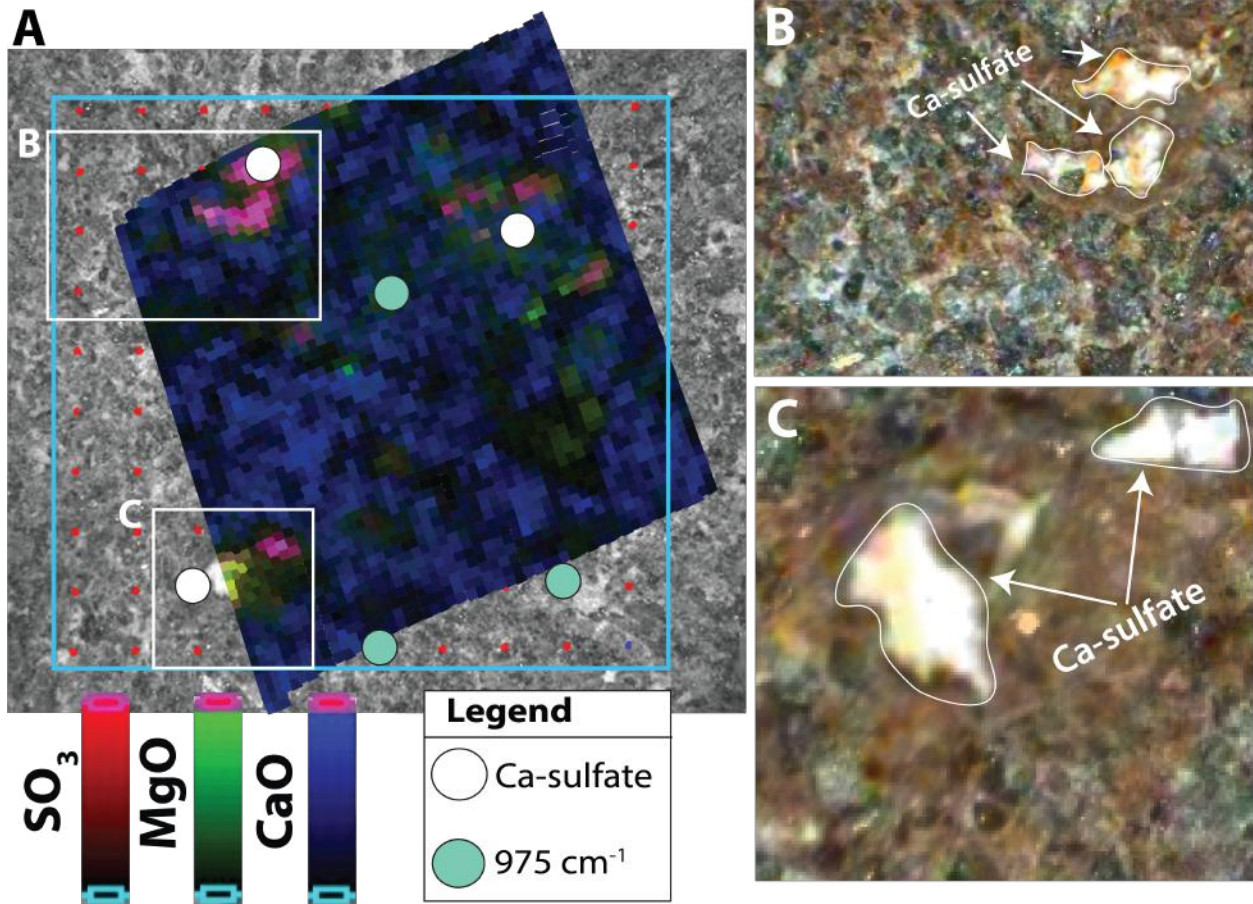
Fig. S3. Hydration feature recorded within Bellegarde sulfates. (A) Average SHERLOC spectrum of the sulfate material within the yellow ROI in panel B showing weak hydration feature at 3560 cm^{-1}. Same spectrum as spectrum no. 1 in Fig. 4. (B) Low SNR Raman map from Fig. 4.E.
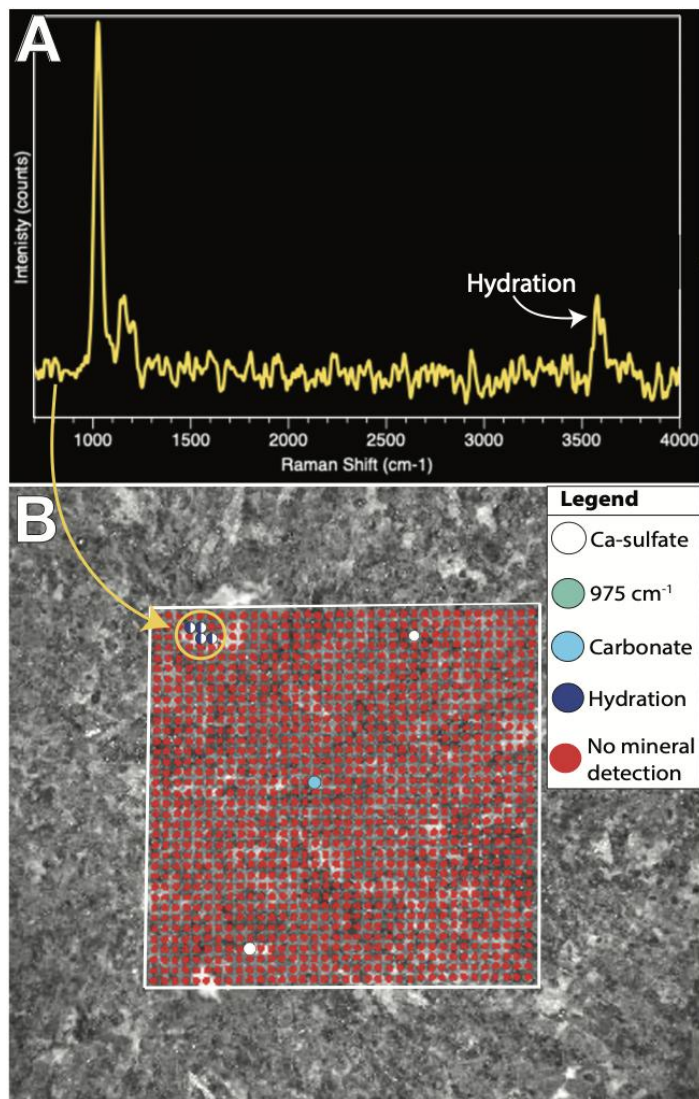
Fig. S4. Comparison between SHERLOC spectra of perchlorate in Guillaumes target and laboratory measurements of a variety of materials. (A,B) Spectrum 5 and spectrum 37 of HDR 2 of Guillaumes from Sol 162, compared to normalised spectra of representative perchlorate, phosphate, sulfate, and carbonate standards, showing that overall spectrum shape is most like that of perchlorate. (C) Secondary peak position plotted against primary peak position for the 4 strongest perchlorate spectra from Guillaumes, compared to all perchlorate and phosphate standards, showing that correlated peak positions are best matched to sodium perchlorate. Vertical dotted line indicates the primary peak position of SHERLOC's possible phosphate detections, whereas grey dots indicate peak positions of perchlorate detections.
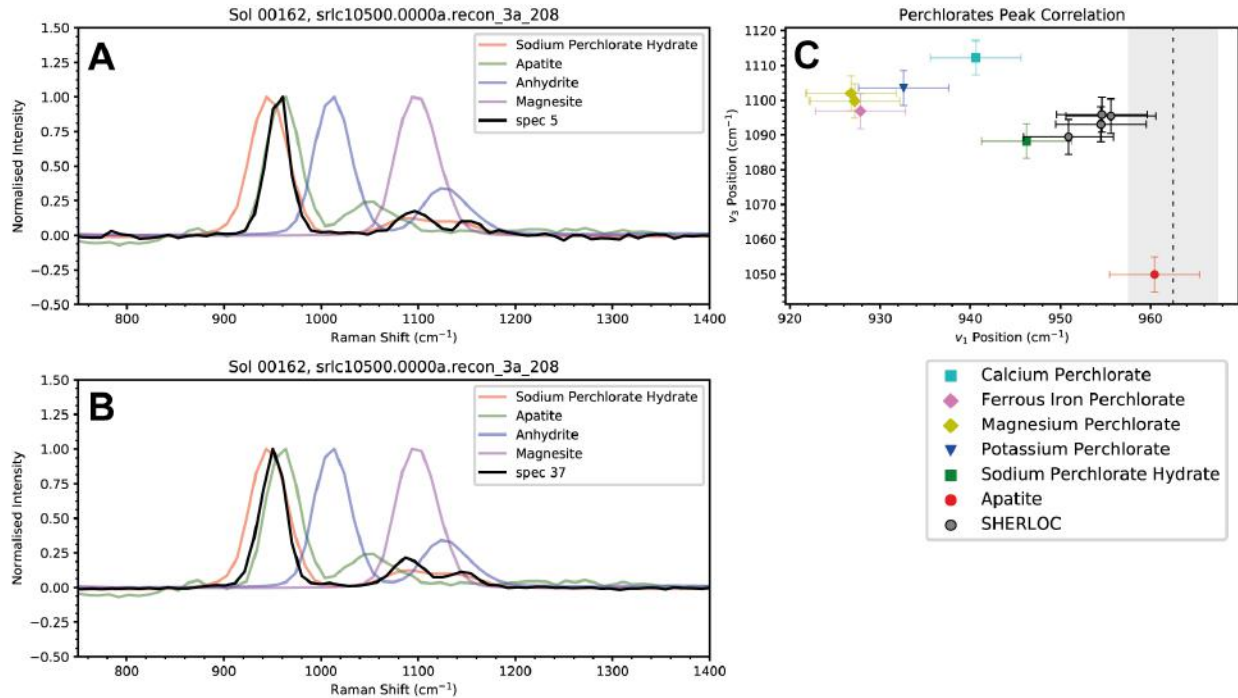
Fig. S5. Elemental chemistry maps of the Bellegarde target produced by the PIXL instrument on the Perseverance rover in comparison to SHERLOC mineral detections. (A) SHERLOC context image of survey scan (white rectangle) and HDR scan (cyan rectangle) superposed on WATSON image of the Bellegarde abraded target from Fig. 4. (B-C) Heatmaps of Cl and Na_2O suggest the presence of a Na- and Cl-rich phase. One SHERLOC 975 cm^{-1} peak correlates with a Na-Cl hotspot. (D) Correlations between SO_3 and CaO suggest the presence of Ca-sulfates (pink), which correlate with Ca-sulfate detections in HDR scans (white circles). (E) Distribution of phosphorus (green) does not obviously correlate with 975 cm^{-1} peaks. (F) Correlations between SiO_2, FeO_T, and Al_2O_3 in the PIXL map show that the primary lithology consists of silicates (cyan and purple) and Fe-oxides (red) and does not correlate with SHERLOC detections. (G) Correlations between SO_3 and CaO suggest the presence of Ca-sulfates (pink), which correlate with Ca-sulfate detections in survey scans (white circles).
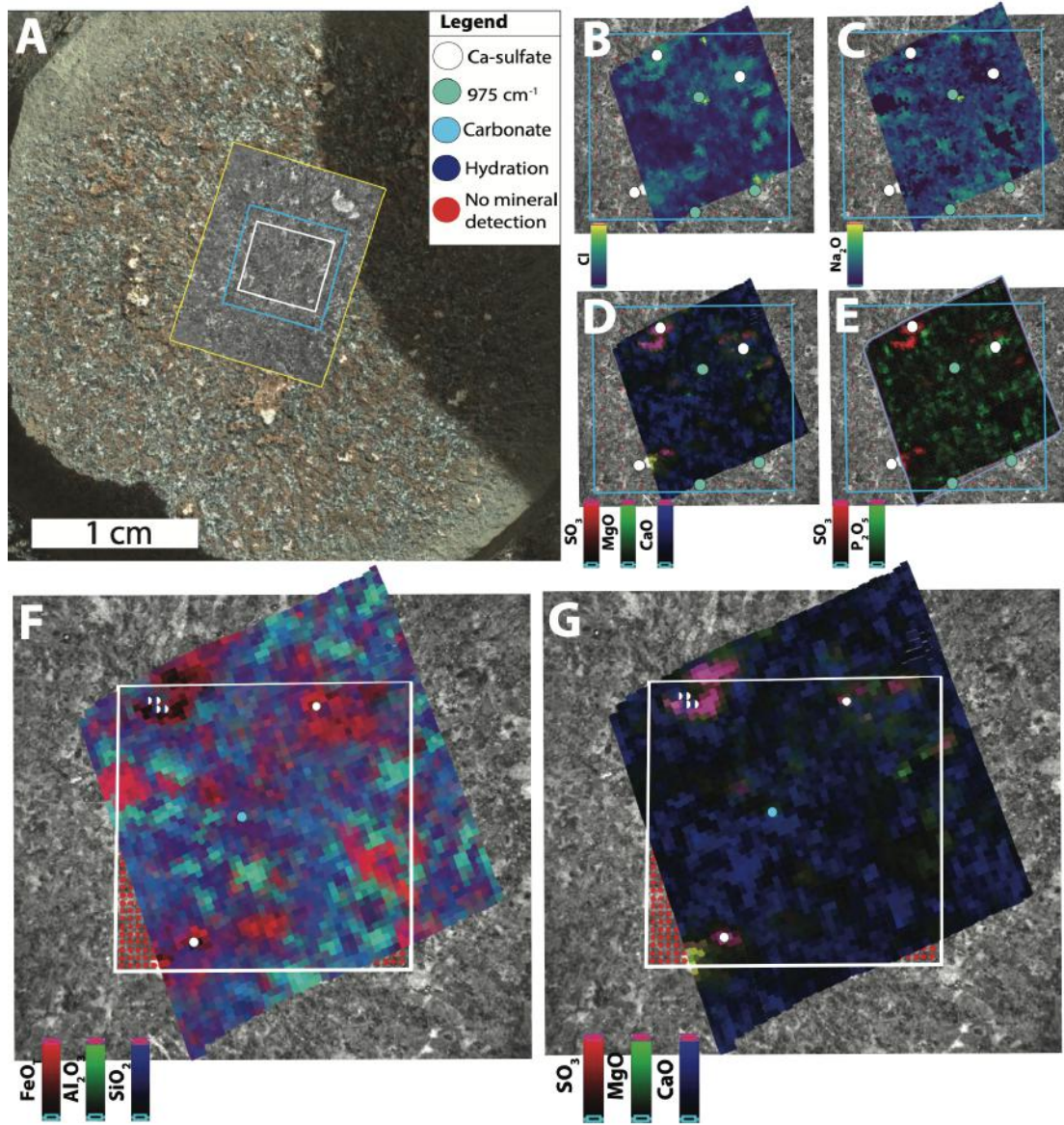
Fig. S6. Elemental chemistry maps of the Guillaumes target produced by the PIXL instrument on the Perseverance rover. (A) PIXL footprint (cyan and purple outline) on PIXL context image showing the location of elemental maps in panel B-G. (B-C) Heatmaps of Cl and Na_2O suggest the presence of a Na- and Cl-rich phase. (D) Spatial relationships between Ca-sulfate (red) and Na- and Cl-rich phases (cyan). (E) Distribution of phosphorus (green) in relation to SO_3 (red). (F) Correlations between SiO_2, FeO_T, and Al_2O_3 showing that the primary lithology consists of silicates (cyan and purple) and Fe-oxides (red). (G) Correlations between SO_3 and CaO suggest the presence of Ca-sulfates (pink).
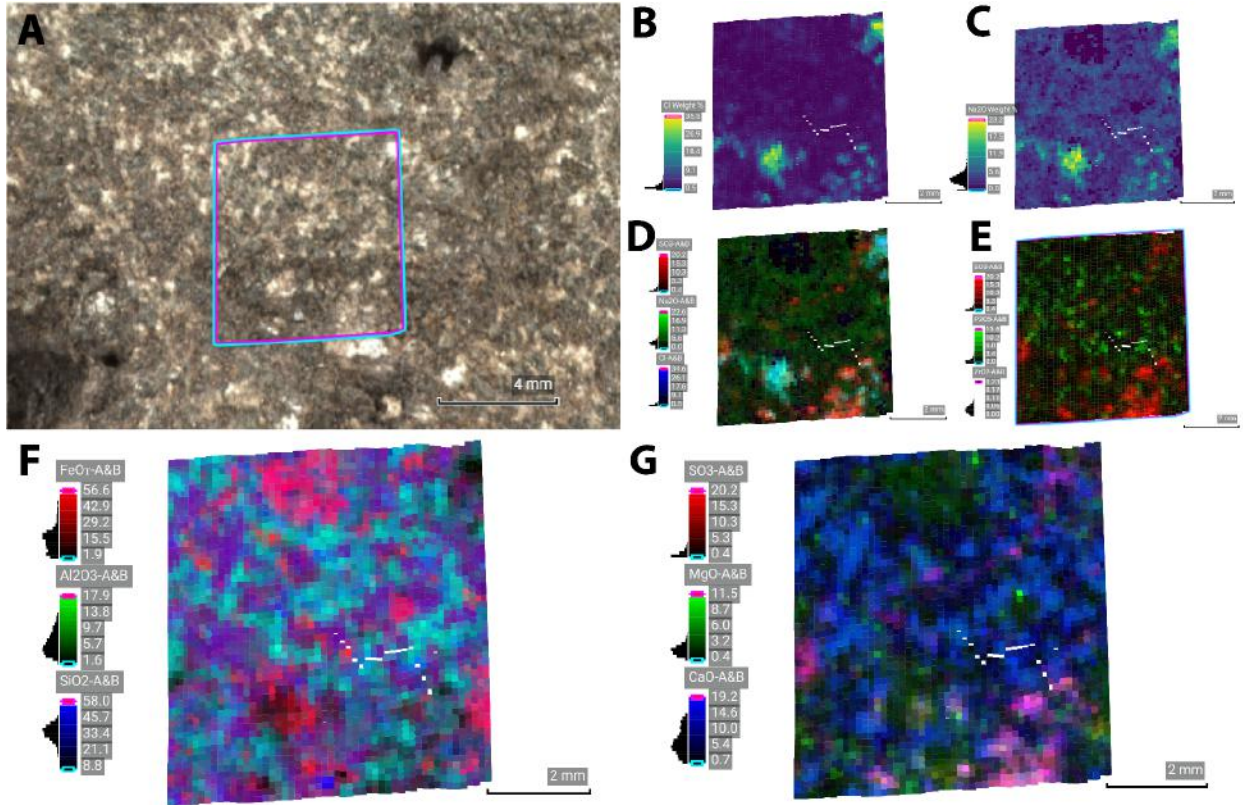
Fig. S7. SHERLOC fluorescence spectra compared to laboratory measurements of simple aromatic organics. Three regions of interest (ROIs) were selected within the fluorescence maps of the three targets, Guillaumes, Bellegarde, and Garde in Fig. 2-4. These demonstrate the variability in fluorescence signatures throughout the rocks that peak at ~275 nm, ~305 nm, and ~340 nm as described in the main text. Below we show laboratory fluorescence measurements of L-phenylalanine, benzoic acid, and naphthalene made with the Brassboard analogue instrument to demonstrate that aromatic organics fluoresce at these same wavelengths. The laboratory measurements show multiple convoluted bands but at the SHERLOC resolution, there would appear as a single broad fluorescence signature similar to those observed in the targets. Note that for Guillaumes spectra, ROI 1 is shown according to the left-hand y-axis, while ROIs 2 and 3 are shown according to the right-hand y-axis.
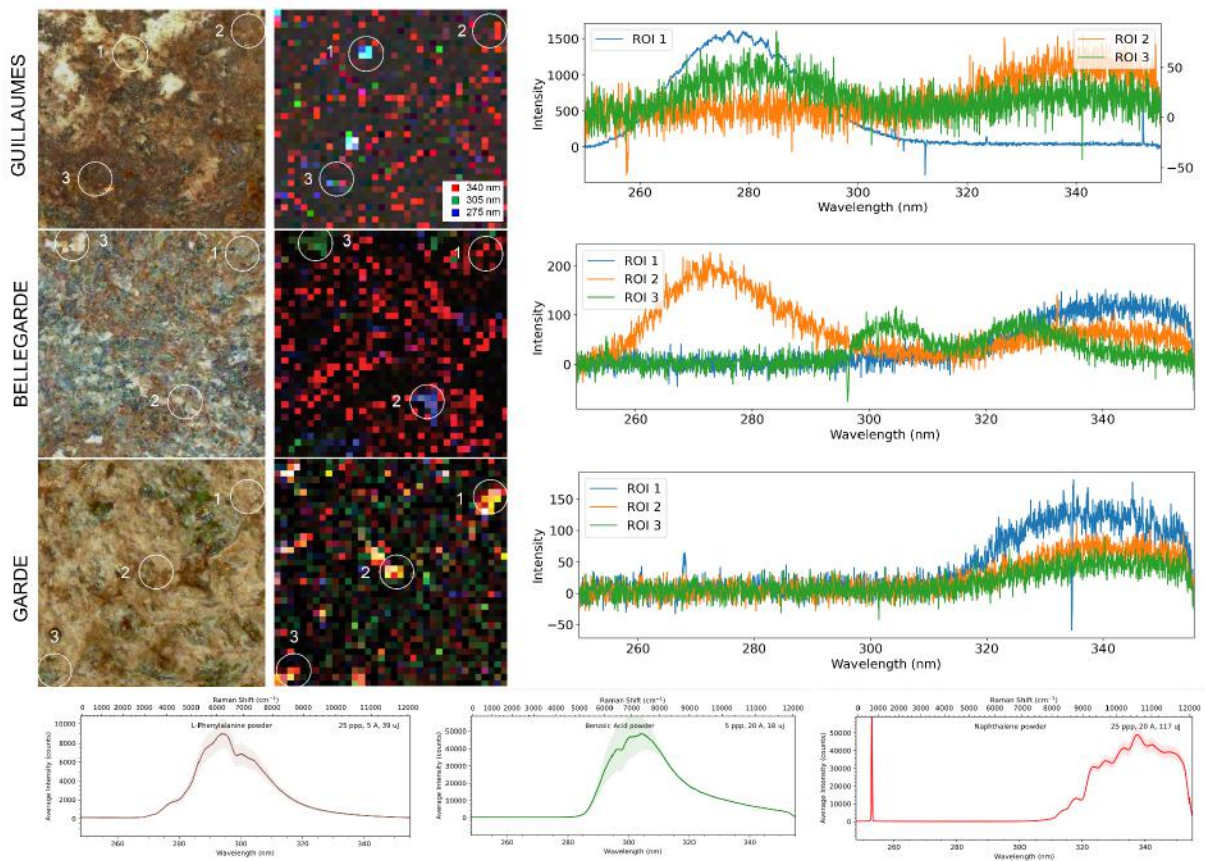
Table S1. Terrestrial apatite from igneous, metamorphic, and/or hydrothermal rocks.
Samples used for measurements displayed in Fig. S8. Details about the apatite mineral identifications and/or compositions are provided in the references *(52-55)*.

Standard Name	Mineral Identification	Location	Ce (ppm)[1]	FWHM (nm)	Peak Center (nm)	REF
Ap 001	Hydroxylapatite	Holly Springs, GA USA	400 ± 20	65.1	350.2	*(52)*
Ap 002	Chlorapatite	Ødegården Verk, Norway	2180 ± 40	51.9	348.5	*(53)*
Ap 003	Fluorapatite	Durango, Mexico	4900 ± 200	47.3	350.2	*(54)*
Ap 004	Fluorapatite	Atlas Mountains, Morocco	2200 ± 200	60.1	358.0	*(54)*
Ap 005	Fluorapatite	Eagle County, CO USA	3880 ± 80	56.7	350.0	*(54)*
Ap 018	Fluorapatite	Lake Baikal, Russia	111 ± 7	63	357.9	*(54)*
Ap 020	Mn-rich Fluorapatite	Unknown Pegmatite, India	1060 ± 90	46.3	333.2	*(54)*
Ap 023	F-OH apatite	Mud Tank Carbonatite, Australia	1760 ± 30	54.6	349.5	*(55)*

[1]**Ce abundances determined by laser ablation inductively coupled mass spectrometry (LA-ICP-MS).**

Fig. S8. SHERLOC fluorescence spectra from the three targets compared to laboratory measurements of phosphates with different trace contents of Ce and aromatic organics. Representative 340 nm fluorescence spectra from the three targets are compared with laboratory measurements of Ce-containing apatites (Ce contents shown in Table S1) and naphthalene. Ce is known to result in fluorescence signatures that overlap in wavelength with those of 2-ring aromatic organics (e.g. naphthalene) (Fig. S7). Note that co-occurring 275 and 285 nm fluorescence in SHERLOC spectra do not have a known inorganic source and are considered organic in origin. Panel D shows a comparison of a spectrum from the Garde target to laboratory measurements of benzene and naphthalene.
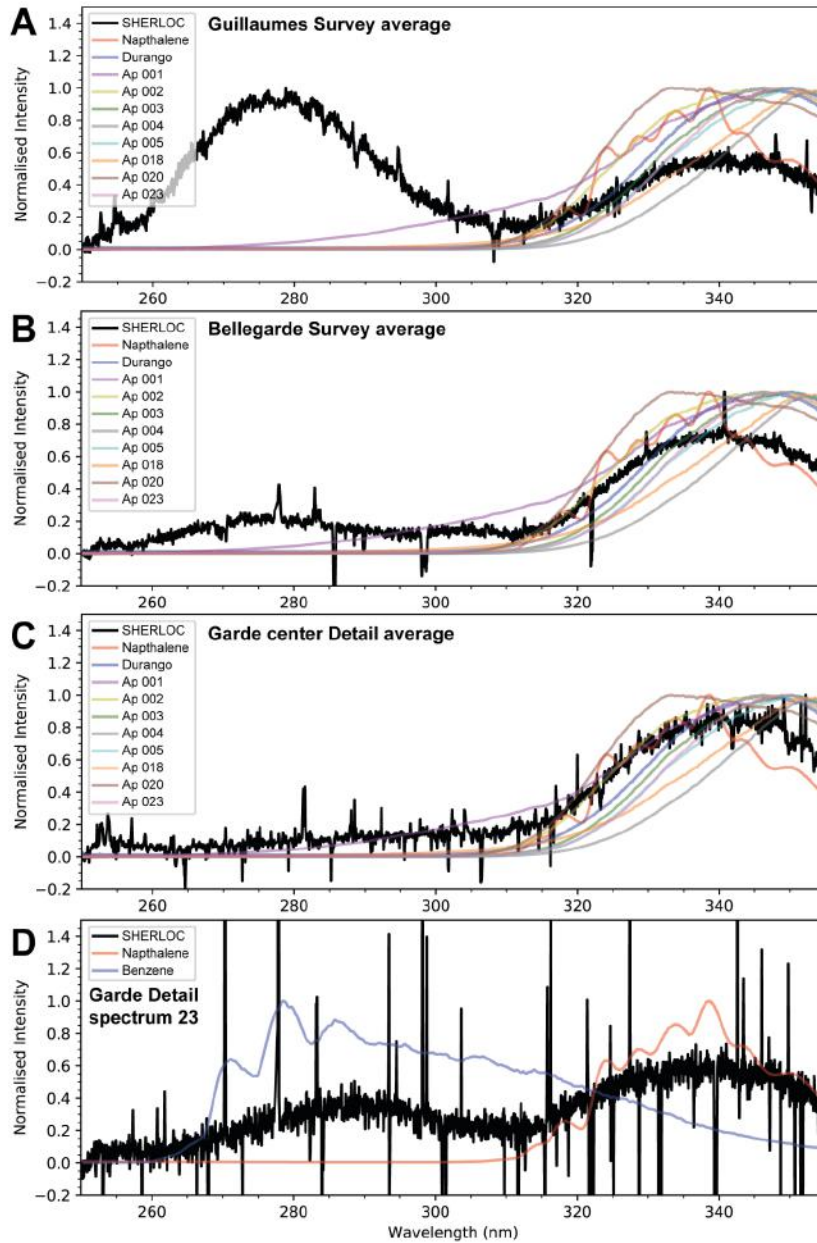
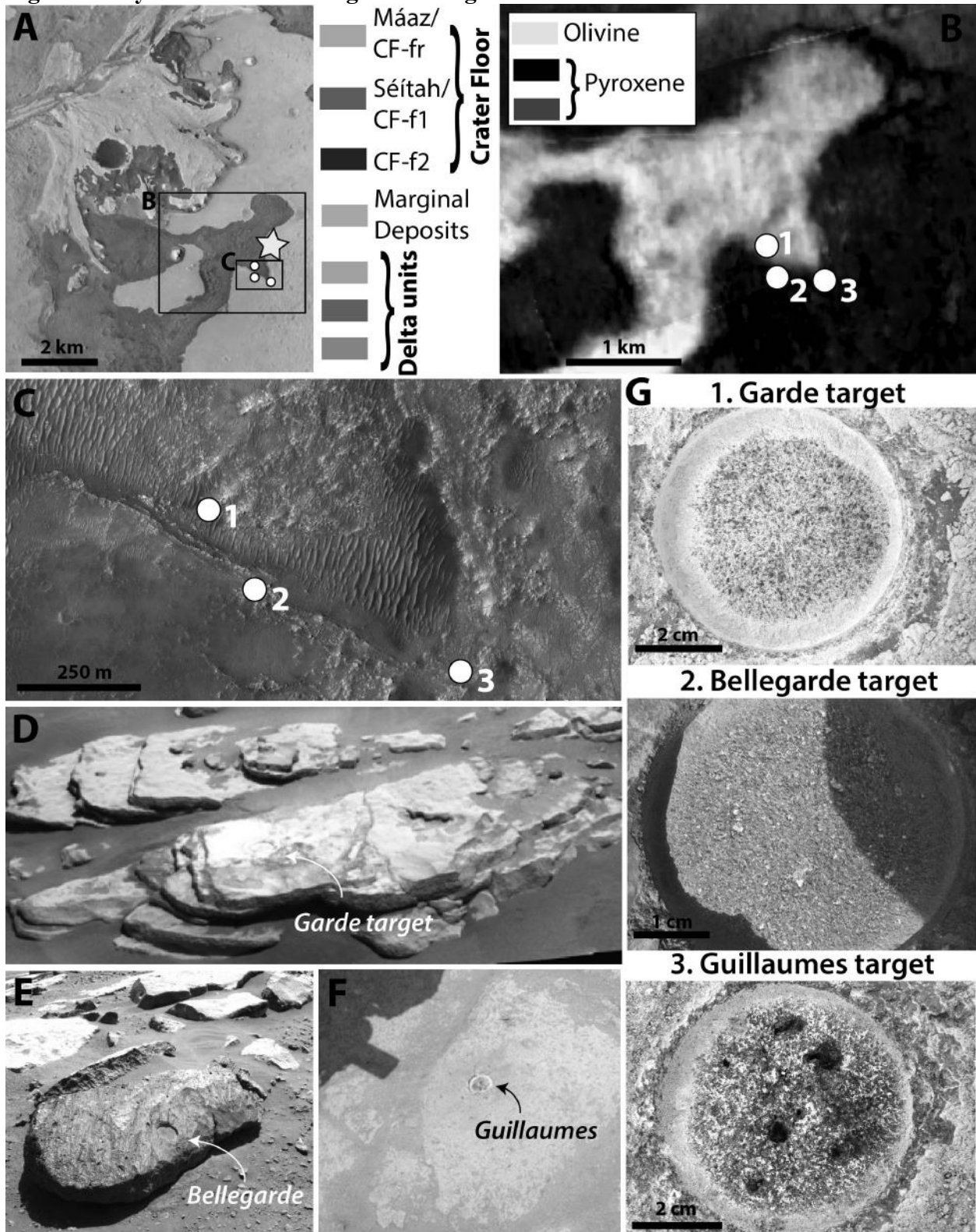**Fig. S9: Grey-scale version of Fig. 1 showing red color-band.**

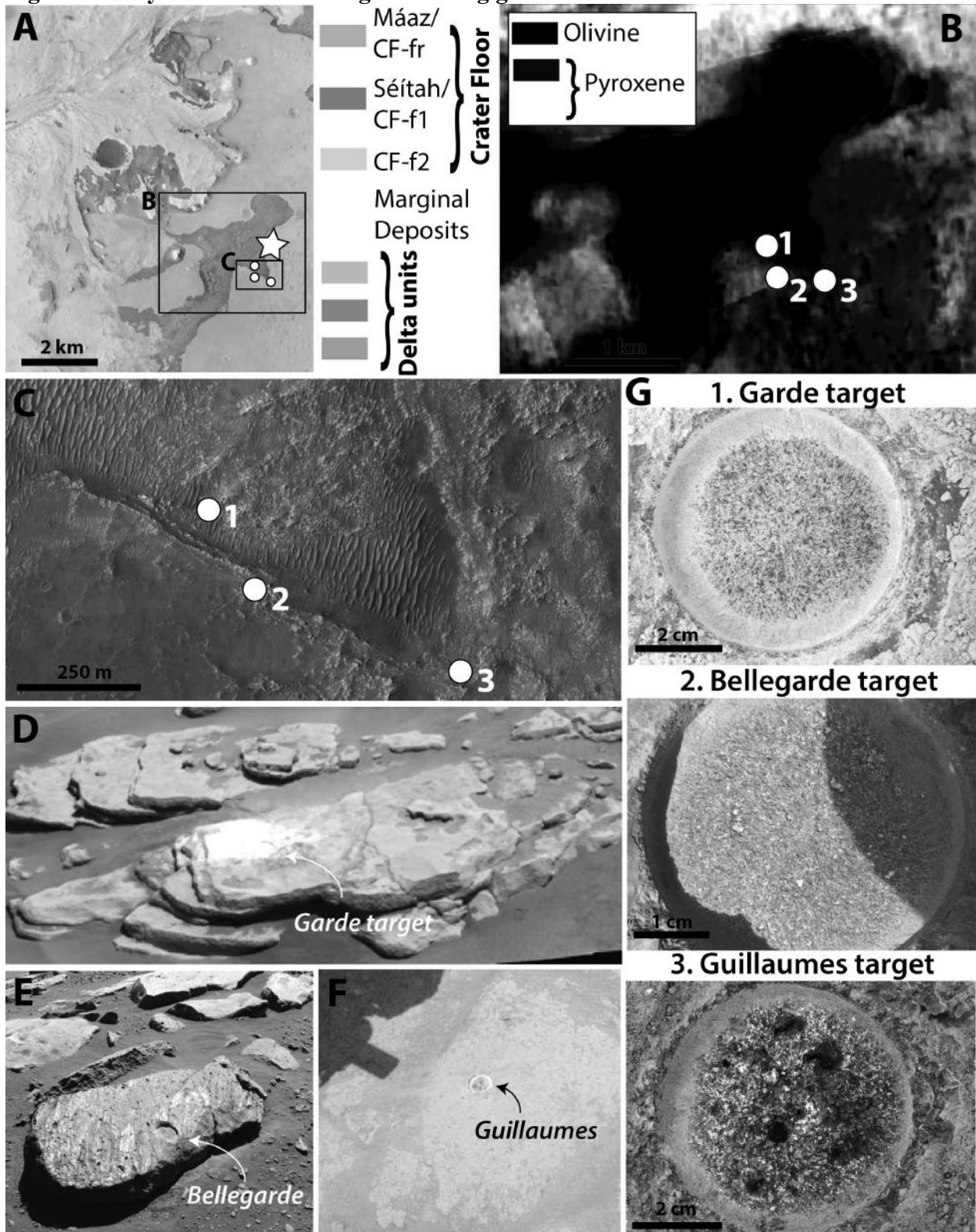**Fig. S10: Grey-scale version of Fig. 1 showing green color-band.**

Fig. S11: Grey-scale version of Fig. 1 showing blue color-band.

Fig. S12: Grey-scale version of Fig. 2 showing red color-band.

Fig. S13: Grey-scale version of Fig. 2 showing green color-band.

Fig. S14: Grey-scale version of Fig. 2 showing blue color-band.

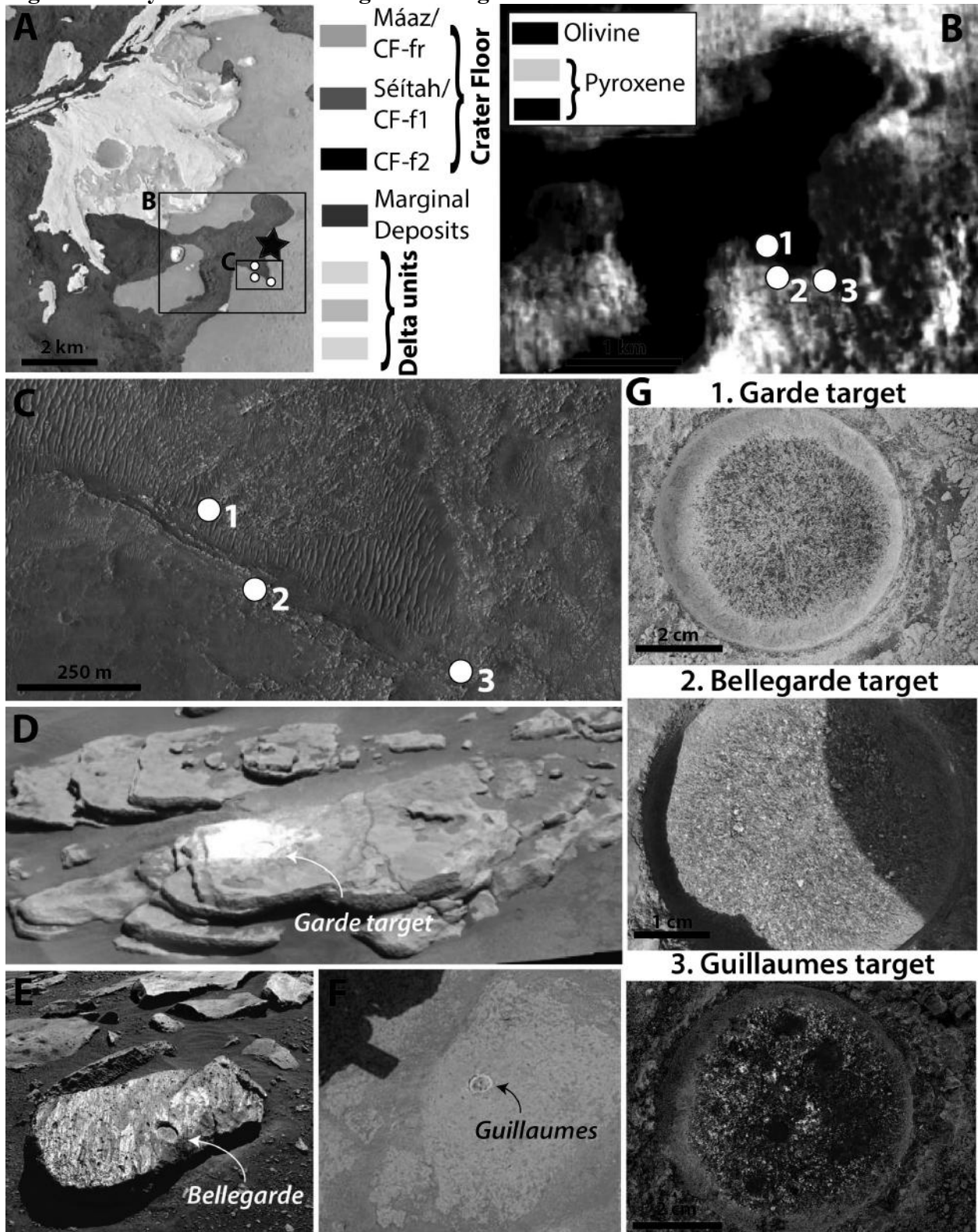**Fig. S15: Grey-scale versions of Garde fluorescence maps from Fig. 2C.**
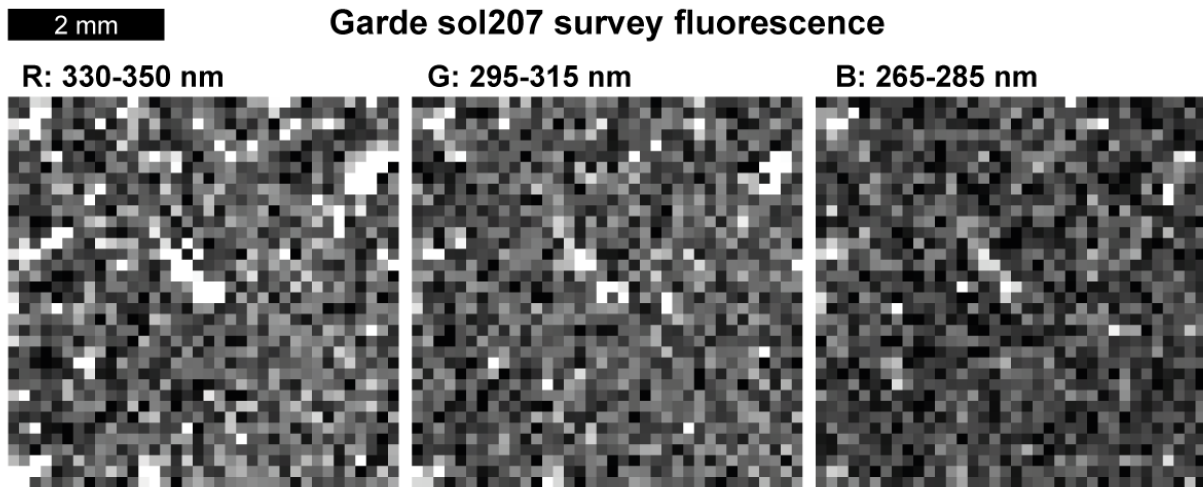
Fig. S16: Grey-scale version of Fig. 3 showing red color-band.
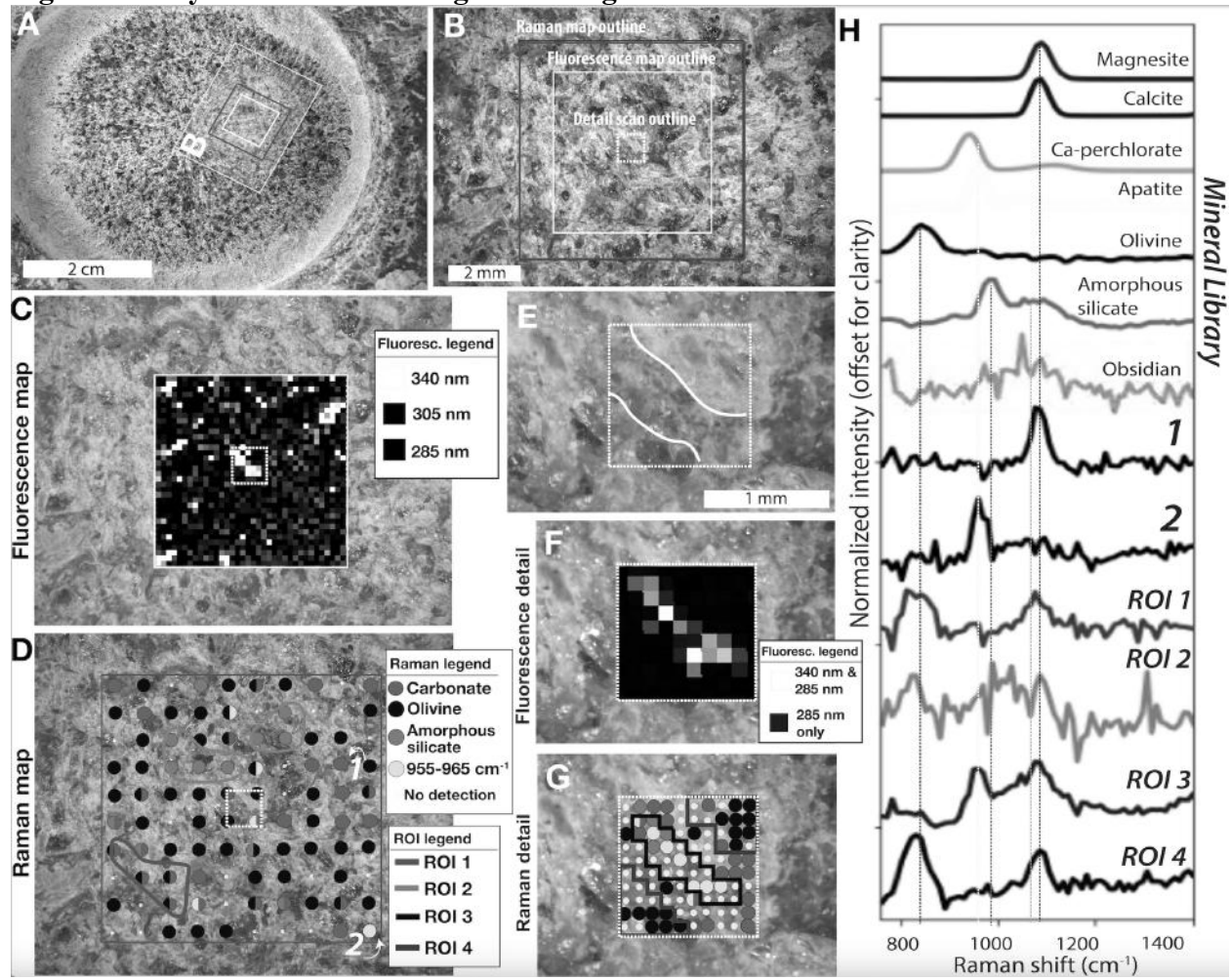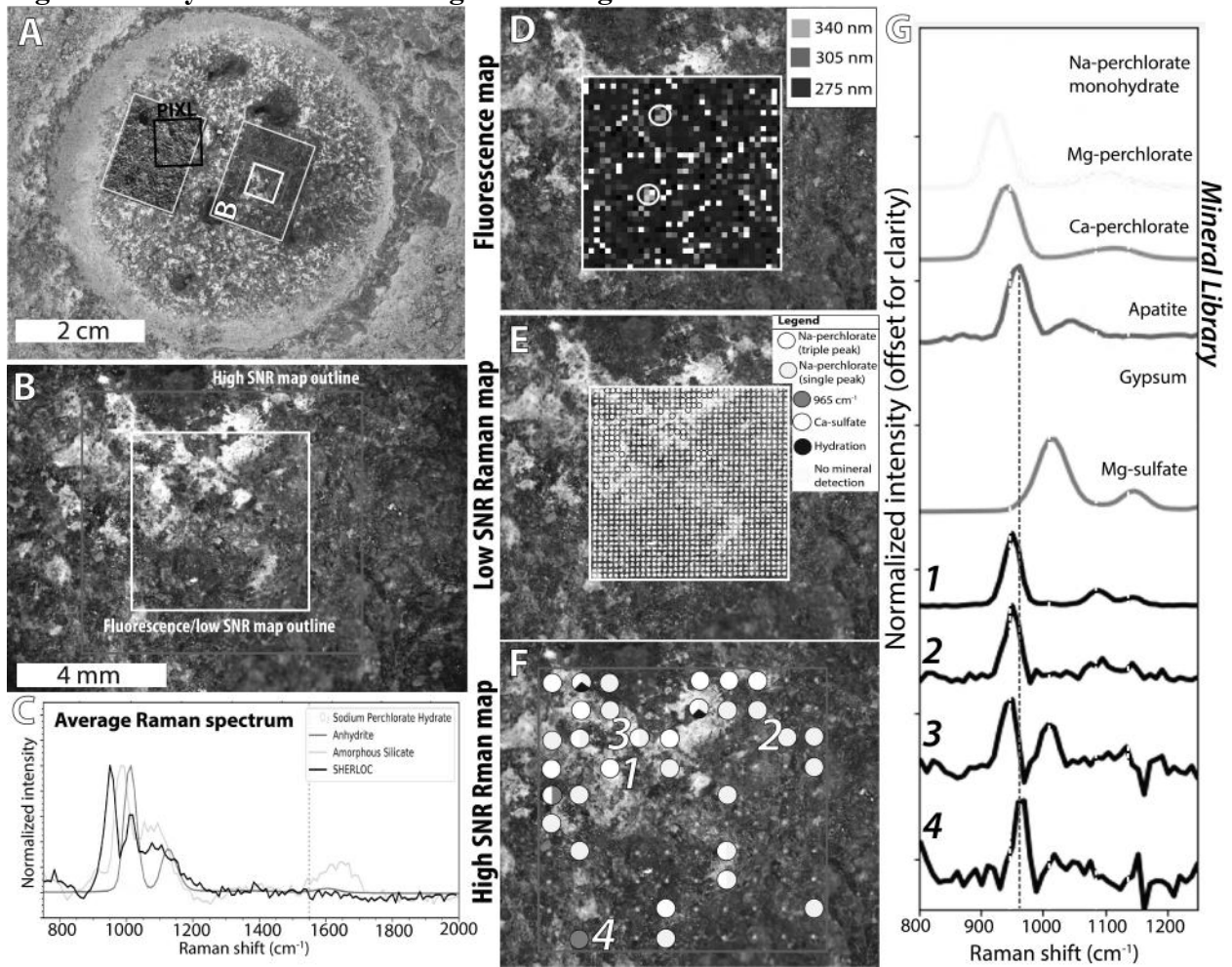
Fig. S17: Grey-scale version of Fig. 3 showing green color-band.
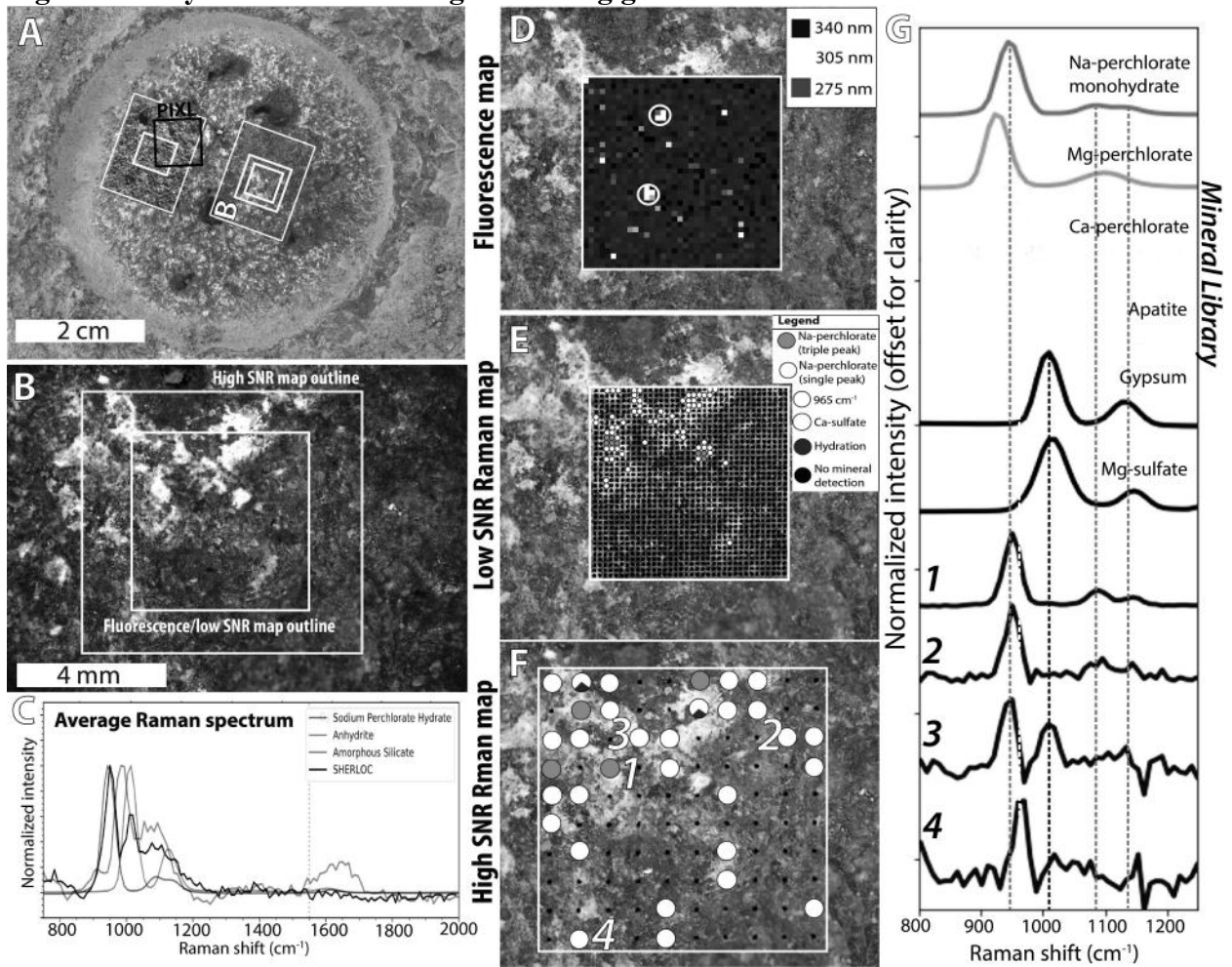
Fig. S18: Grey-scale version of Fig. 3 showing blue color-band.
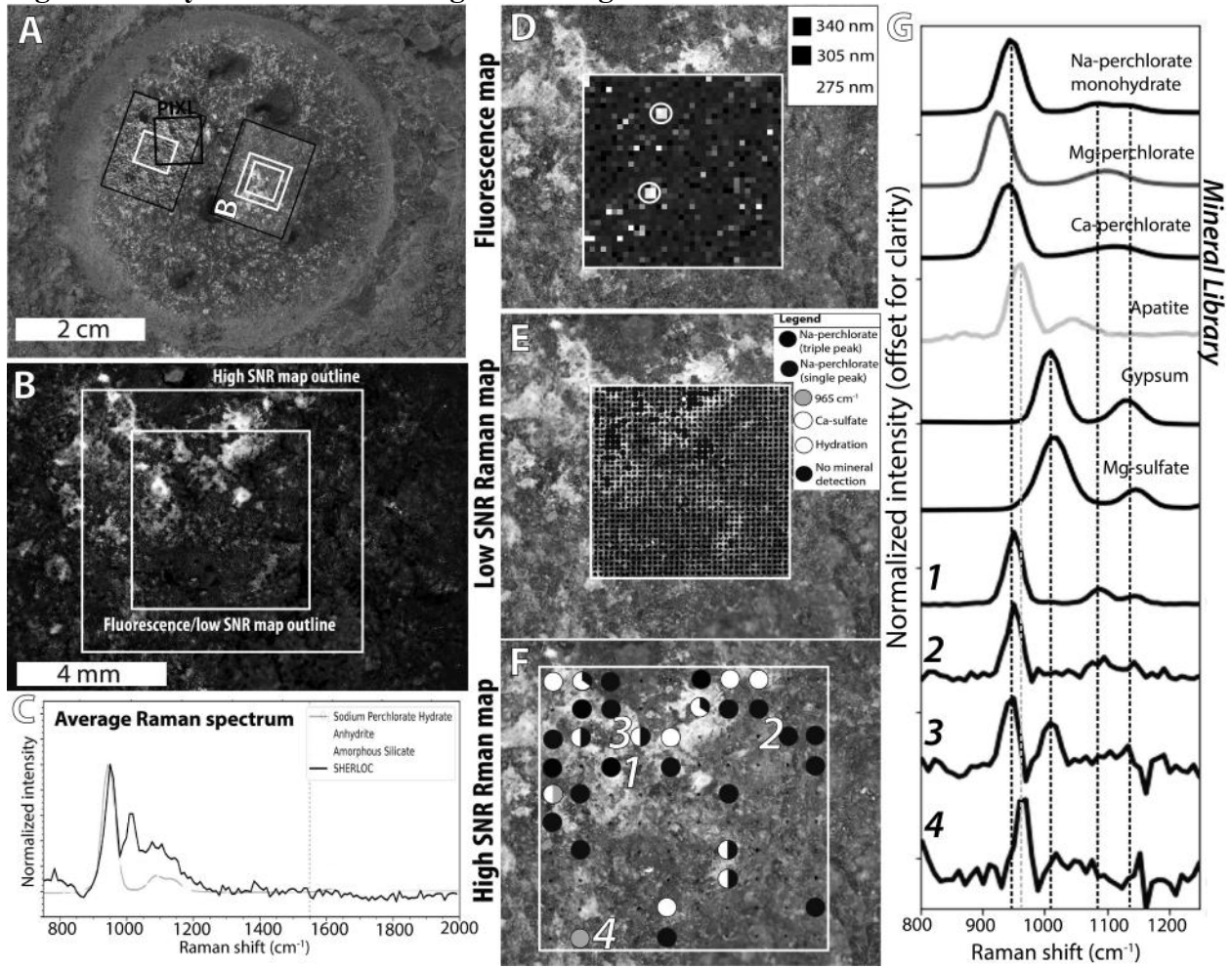
Fig. S19: Grey-scale versions of Guillaumes fluorescence maps from Fig. 3D.
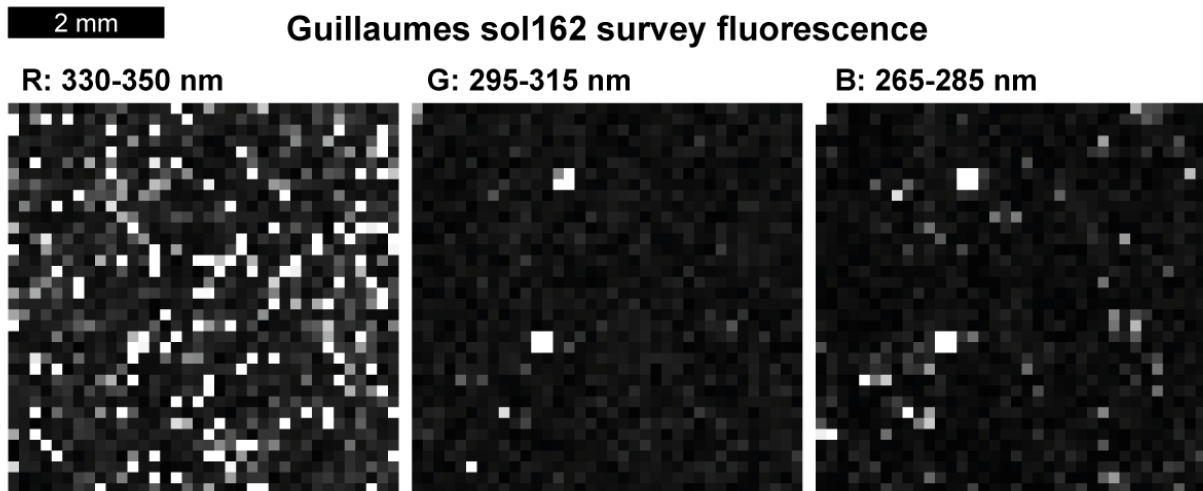
Fig. S20: Grey-scale version of Fig. 4 showing red color-band.
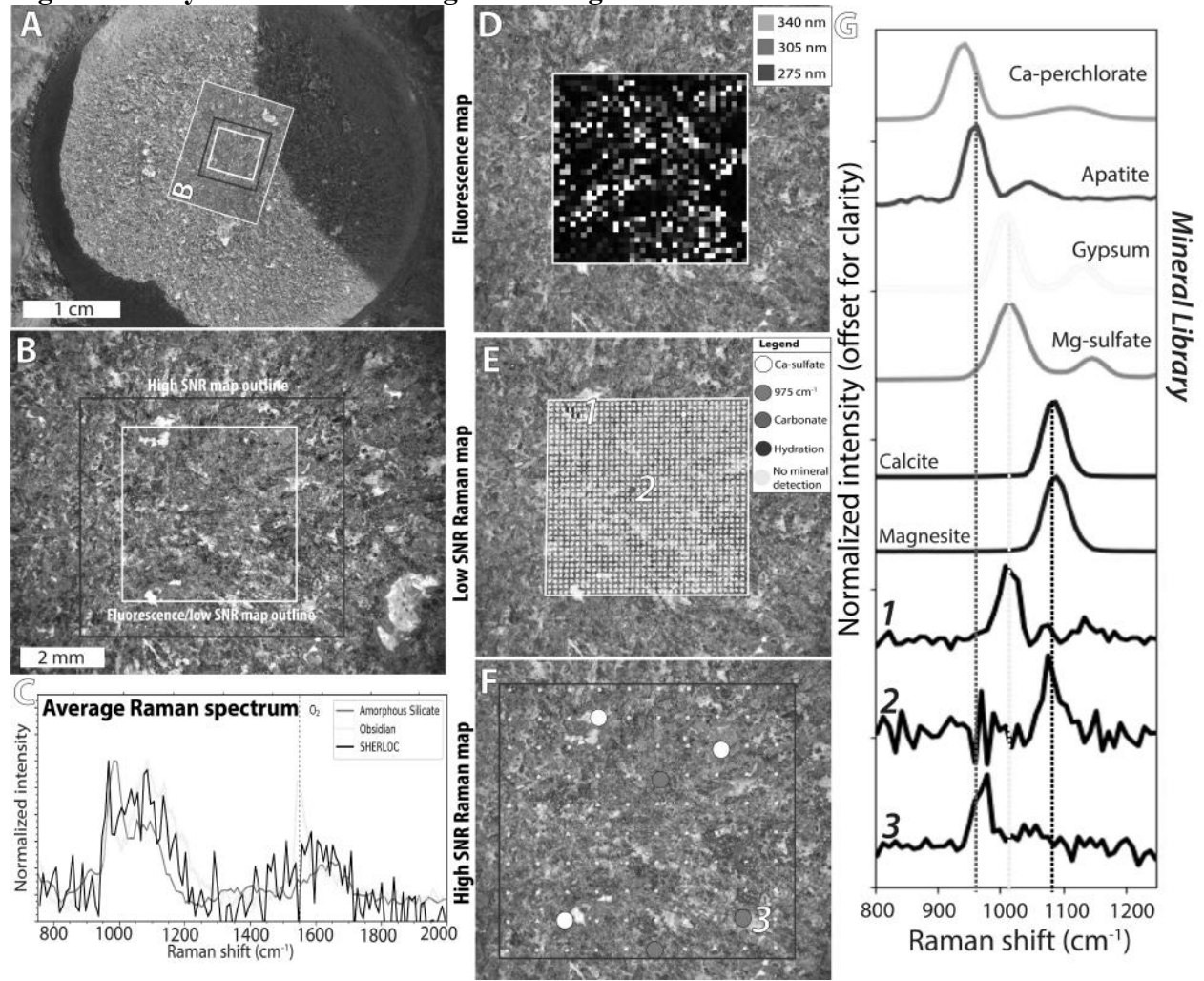
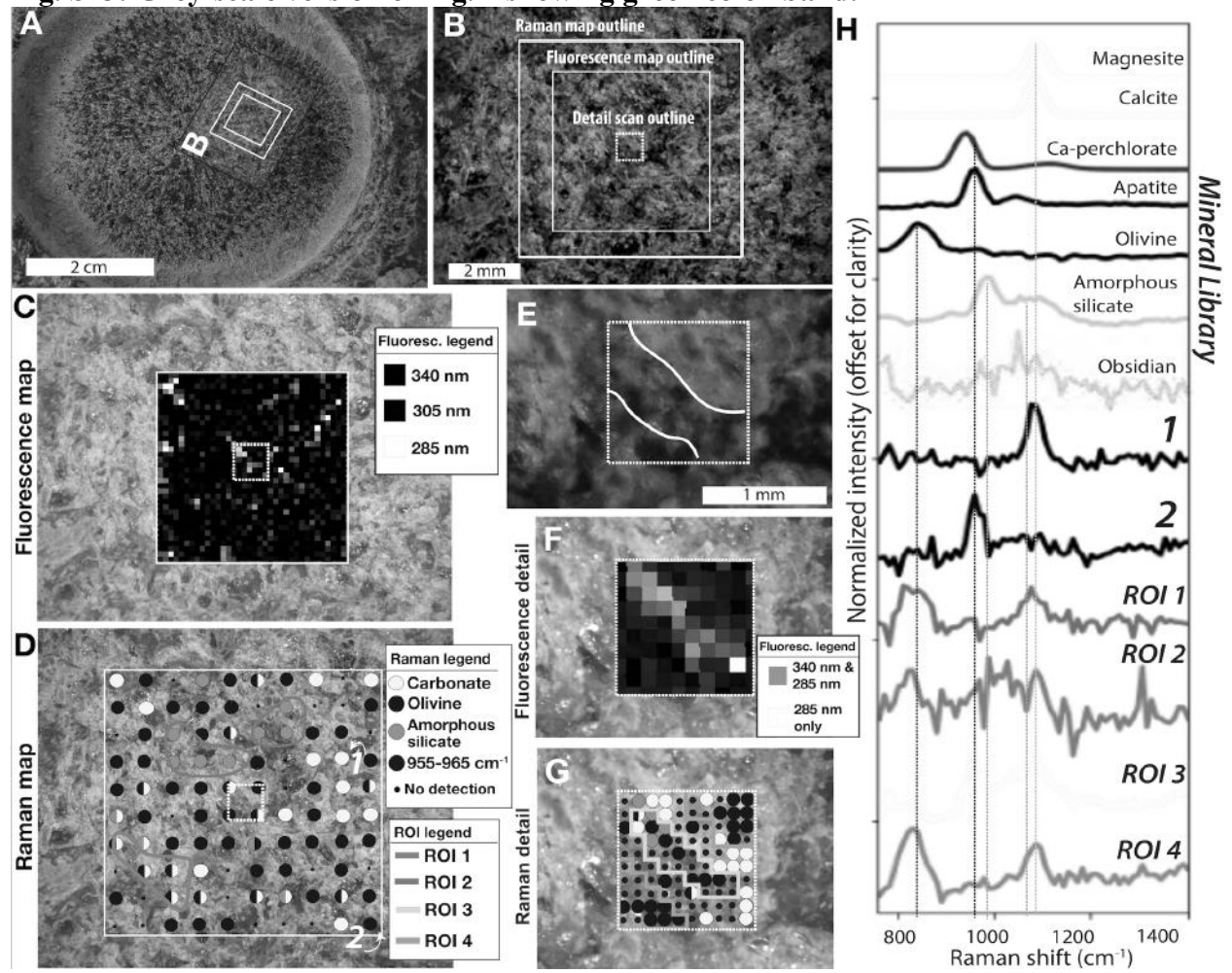**Fig. S21: Grey-scale version of Fig. 4 showing green color-band.**

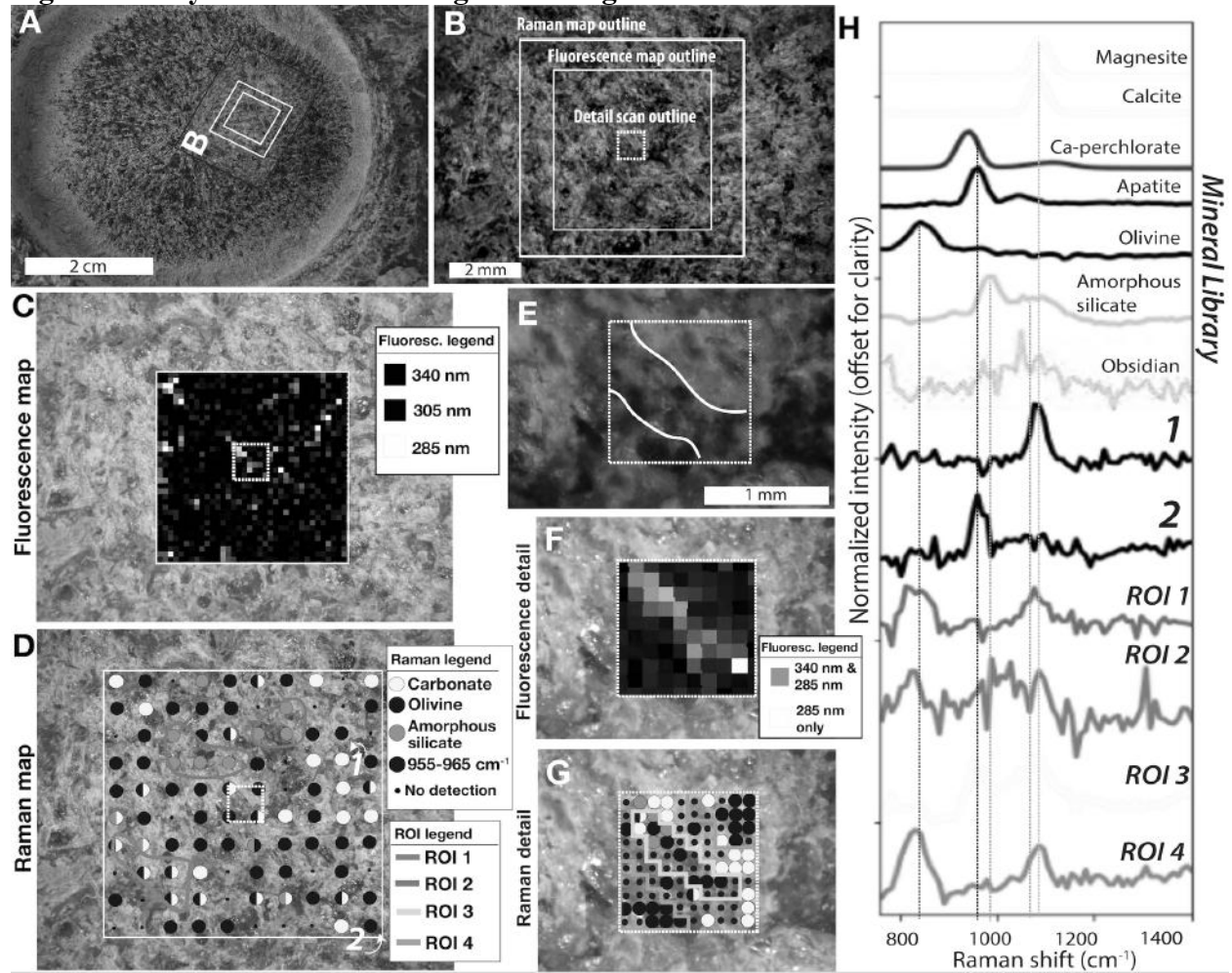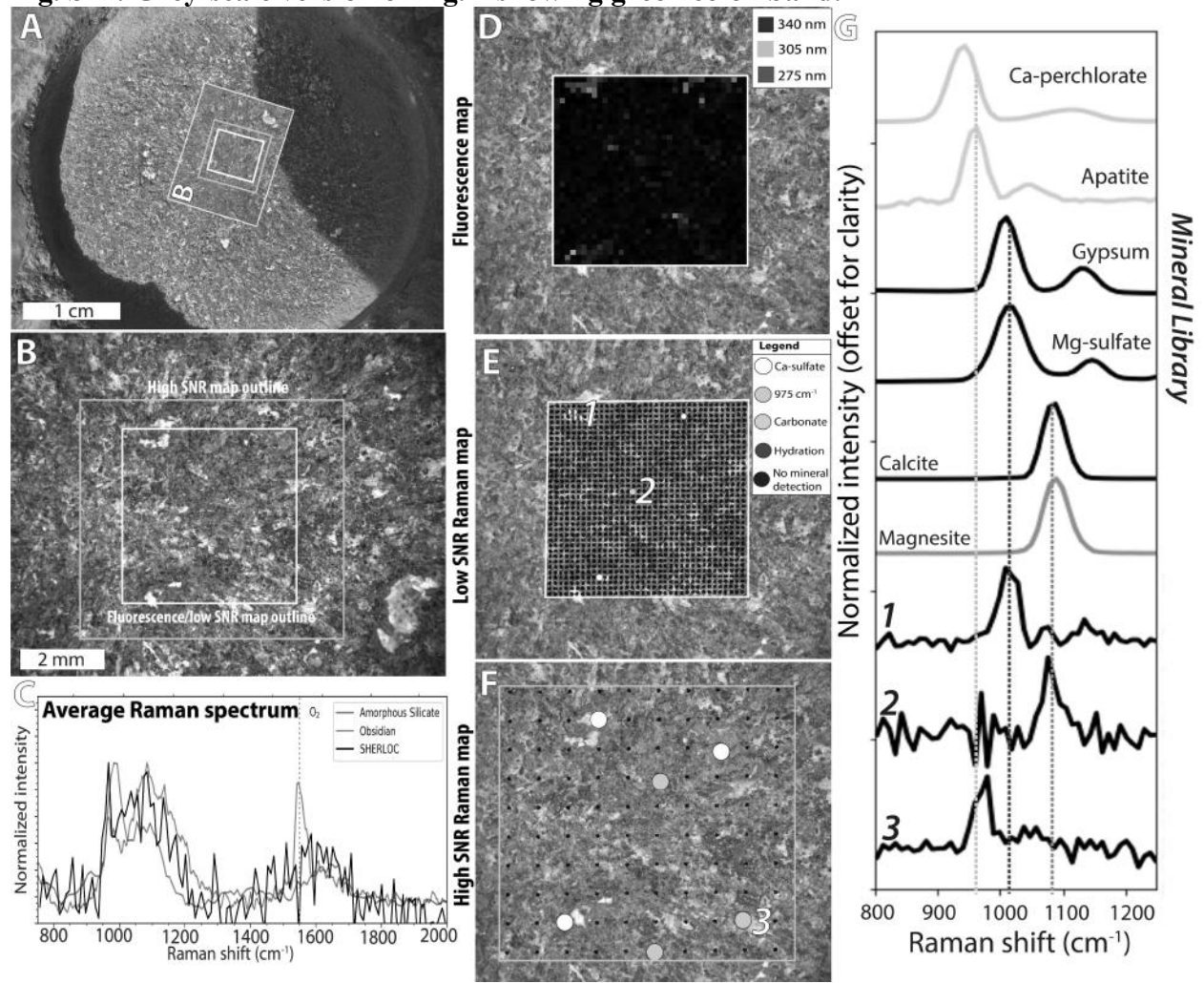**Fig. S22: Grey-scale version of Fig. 4 showing blue color-band**
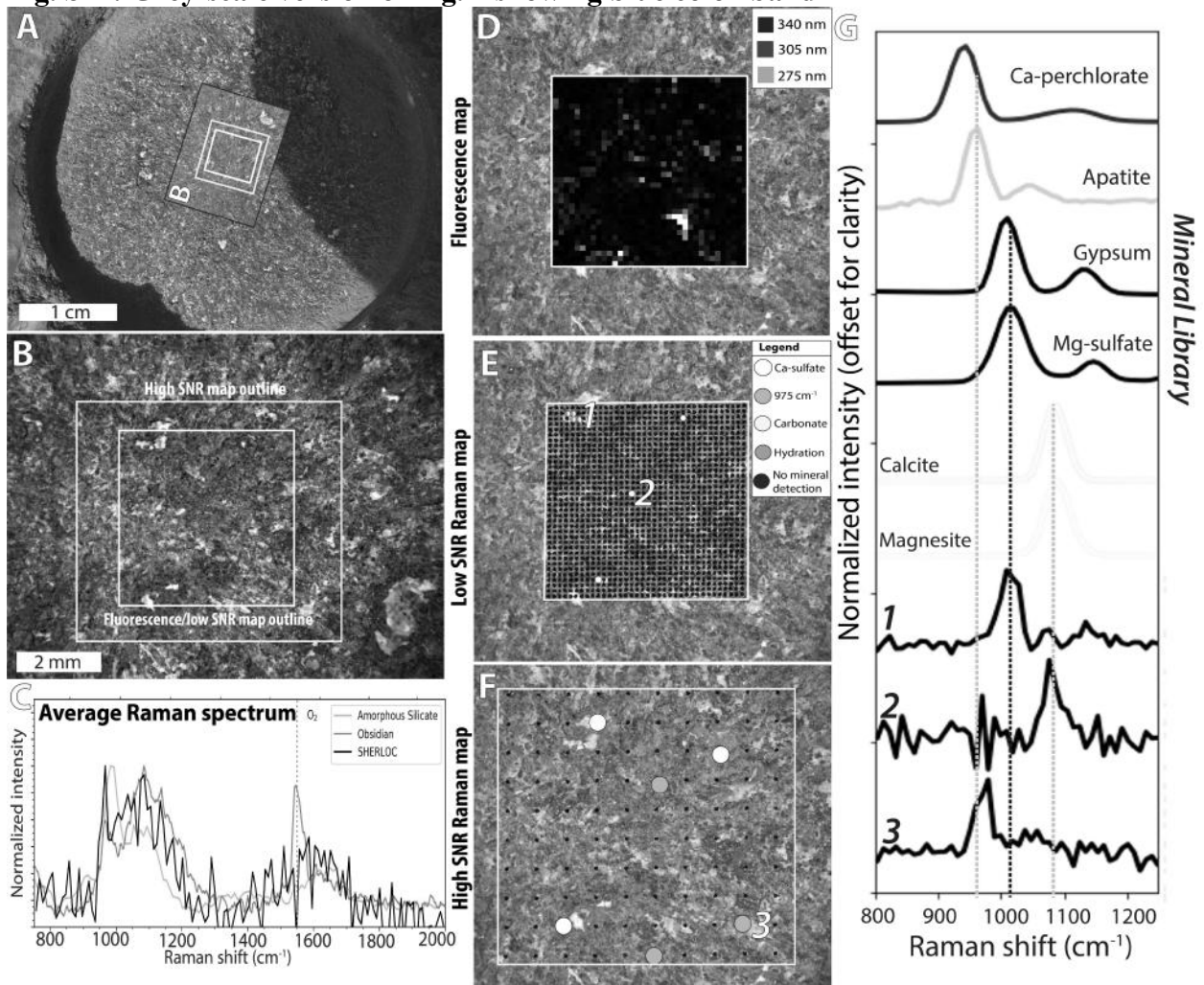
Fig. S23: Grey-scale versions of Bellegarde fluorescence maps from Fig. 4D.

A — Crater Floor units legend:
- Máaz/CF-fr
- Séítah/CF-f1
- CF-f2
- Marginal Deposits
- Delta units

B — Olivine / Pyroxene spectral map

C — target locations 1, 2, 3

D — *Garde target*

E — *Bellegarde*

F — *Guillaumes*

G
1. Garde target
2. Bellegarde target
3. Guillaumes target

A 2 cm

B Raman map outline
Fluorescence map outline
Detail scan outline
2 mm

C Fluorescence map
Fluoresc. legend
- 340 nm (red)
- 305 nm (green)
- 285 nm (blue)

D Raman map
Raman legend
- Carbonate
- Olivine
- Amorphous silicate
- 955-965 cm^{-1}
- No detection

ROI legend
- ROI 1
- ROI 2
- ROI 3
- ROI 4

E 1 mm

F Fluorescence detail
Fluoresc. legend
- 340 nm & 285 nm
- 285 nm only

G Raman detail

H *Mineral Library*
Normalized intensity (offset for clarity)

Magnesite
Calcite
Ca-perchlorate
Apatite
Olivine
Amorphous silicate
Obsidian
1
2
ROI 1
ROI 2
ROI 3
ROI 4

Raman shift (cm^{-1})
800   1000   1200   1400

A PIXL · B · 2 cm

B High SNR map outline · Fluorescence/low SNR map outline · 4 mm

C Average Raman spectrum
- Sodium Perchlorate Hydrate
- Anhydrite
- Amorphous Silicate
- SHERLOC

Normalized intensity — Raman shift (cm⁻¹): 800, 1000, 1200, 1400, 1600, 1800, 2000

D Fluorescence map
- 340 nm
- 305 nm
- 275 nm

E Low SNR Raman map
Legend
- Na-perchlorate (triple peak)
- Na-perchlorate (single peak)
- 965 cm⁻¹
- Ca-sulfate
- Hydration
- No mineral detection

F High SNR Rman map

G Mineral Library
- Na-perchlorate monohydrate
- Mg-perchlorate
- Ca-perchlorate
- Apatite
- Gypsum
- Mg-sulfate
- 1
- 2
- 3
- 4

Normalized intensity (offset for clarity) — Raman shift (cm⁻¹): 800, 900, 1000, 1100, 1200

A — 1 cm

B — High SNR map outline / Fluorescence/low SNR map outline — 2 mm

C — Average Raman spectrum — O₂ — Amorphous Silicate, Obsidian, SHERLOC — Normalized intensity — Raman shift (cm⁻¹)

D — Fluorescence map — 340 nm, 305 nm, 275 nm

E — Low SNR Raman map — Legend: Ca-sulfate, 975 cm⁻¹, Carbonate, Hydration, No mineral detection — 1, 2

F — High SNR Raman map — 1, 3

G — Mineral Library — Ca-perchlorate, Apatite, Gypsum, Mg-sulfate, Calcite, Magnesite — 1, 2, 3 — Normalized intensity (offset for clarity) — Raman shift (cm⁻¹)